SIMULATION OF FOLD-LINE STIFFNESS IN DEPLOYABLE MEMBRANES

Buwaneth Yasara Dharmadasa

168019K

Thesis submitted in partial fulfilment of the requirements for the
degree Master of Science in Civil Engineering

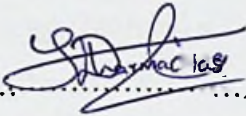Department of Civil Engineering

University of Moratuwa

Sri Lanka

July 2017

DECLARATION

I declare that this is my own work and this thesis does not incorporate without acknowledgement any material previously submitted for a Degree or Diploma in any other University or institute of higher learning and to the best of my knowledge and belief it does not contain any material previously published or written by another person except where the acknowledgement is made in the text.

Also, I hereby grant to University of Moratuwa the non-exclusive right to reproduce and distribute my thesis, in whole or in part in print, electronic or other medium. I retain the right to use this content in whole or part in future works (such as articles or books)

....   Date: 17th July 2017

B.Y.Dharmadasa

The above candidate has carried out research for the Masters under my supervision.

UOM Verified Signature ....   Date: 17th July 2017

Dr.H.M.Y.C.Mallikarachchi

ABSTRACT

New designs for space structures such as solar sails and star shades are based on architectures that follow folding and packaging of thin membranes. By leveraging recent advances in origami science, it is possible to design structures in which folded thin membranes deploy following a predetermined and robust path. Design and product optimization of deployable space structures are limited by complex environmental conditions experienced by them. However virtual simulations can be the perfect solution provided proper idealization techniques are followed.

Presence of fold-lines alter the geometrical and mechanical properties of thin membranes which have not being accounted in previous virtual simulations. Two major characteristics identified was the self-opening of the membrane to an equilibrium angle (defined as neutral angle) and the rotational spring stiffness of the membrane at the fold-line.

An experimental study was devised to investigate the variation of fold-line stiffness while varying the neutral angles and membrane thickness for Kapton HN polyimide. A linear empirical relationship between resistive moment and fold-angle is proposed for each thickness.

Self-opening and subsequent unfolding of a single fold was modelled using commercial finite element package, Abaqus/Explicit. Fold-line characteristics were represented with rotational spring connector elements defined between two shell portions. Compared to common idealization approaches (perfect hinge and perfect weld), rotational spring connectors were able to accurately predict the deformation profile and unfolding forces.

Finally, the developed fold idealization technique was applied in an experimental case study of a deploying solar sail. It was shown that neglecting fold-line stiffness underestimate the deploying force of the sail.

Key words: *Folded Membranes; Crease Response; Solar Sails; Finite Element Simulations*

DEDICATION

To my parents, without whom none of this would be possible.

ACKNOWLEDGEMENT

TABLE OF CONTENTS

LIST OF FIGURES

LIST OF TABLES

NOMENCLATURE

List of Symbols

ε_{max}	- Fraction of critical damping in highest mode
θ	- Current angle between fold-lines
θ^*	- Folding ratio
υ	- Poisson's ratio
ρ	- Material density
φ	- Neutral angle between fold-lines
ω_{max}	- Highest Eigen value of the model
C_d	- Dilation wave speed
C_v	- Viscous pressure coefficient
D	- Current diameter of the solar sail
D_f	- Initial diameter (before folding) of the solar sail
E	- Young's Modulus
E_f	- Frictional dissipation energy
E_i	- Internal energy (elastic, inelastic, "artificial" strain energy)
E_{ke}	- Kinetic energy
E_{tot}	- Total energy in the system
E_{vd}	- Energy absorbed by viscous dissipation
E_w	- Work of external forces
k	- Gradient of the graph
l	- Membrane length between two folds
L^*	- Characteristic origami length
M	- Resistive moment at the fold-line
n	- Number of sides of a polygon
R_i	- Rotations about i^{th} axis
T	- Tensile load in the membrane due to fold
t	- Time period
U_i	- Translations in i^{th} direction
x	- Distance to the fold-line from the boundary of membrane

List of Abbreviations

CPU	- Central Processing Unit
FEA	- Finite Element Analysis
IKAROS	- Interplanetary Kite-craft Accelerated by Radiation Of the Sun
JAXA	- Japanese Aerospace Exploration Agency
NASA	- National Aeronautics and Space Administration
RP	- Reference Point

CHAPTER I

1. INTRODUCTION

The concept of deployable/expandable structures, where a structure has the ability to reconfigure its geometry from a compact state to a much larger operational configuration has become increasingly popular among engineers. An umbrella is the simplest example for a deployable structure where it can be compacted to fit into a small backpack, but can also be deployed to provide cover for a person on a rainy day. Similar concepts are widely used for many engineering applications including space industry.

Limited volume of a launch vehicle is one of the major constraints for designing space structures such as solar sails or star shades which needs to cover a large surface area (Sickinger & Breitbach, 2004). Solar sail is a low cost, innovative design that supersedes traditional satellites for long range missions. In contrast to traditional satellites, solar sails can generate a thrust using solar energy where a sail with a larger surface area can produce a higher thrust. The estimated surface area of the sails can vary up to hundreds of metres in diameter (NASA, 2005). A star shade is similar to a gigantic umbrella protecting satellites that orbit around bright stars from harmful rays, allowing its cameras to capture surrounding celestial bodies. Figure 1.1 is an artist impression of a sun shade protecting the satellite from a star.

1.1. Foldable Membranes

Micron scale thin membranes have been used to design structures where a surface area greater than a football field needs to be wrapped around a hub of 2 m diameter. Origami science have been applied to develop wrapping patterns that ensure smooth deployment of the sail once it reaches the orbit. The deploying technique is also crucial for mission's success since complex unfolding methods may need additional motors or can get jammed in the deployment process (Sakamoto, et al., 2014). Figure 1.2 demonstrates the unfolding process of IKAROS (Interplanetary Kite-craft Accelerated by Radiation of the Sun) solar sail which uses centrifugal forces to deploy its sail.
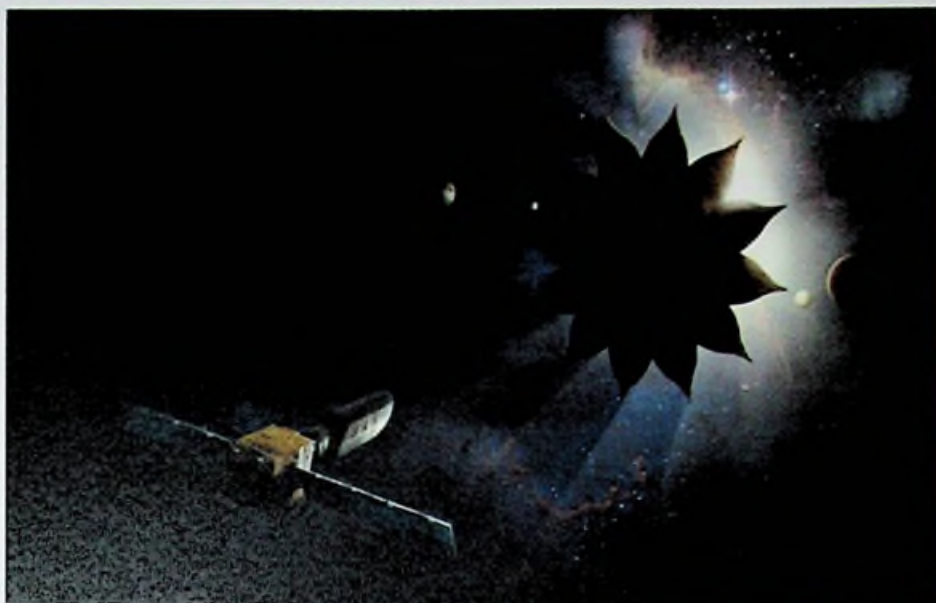
Figure 1.2: An artist's impression of a star shade
(Source*:   https://www.spaceanswers.com/futuretech/solar-probe-plus-nasas-sun-skimming-spacecraft/*)

The term *origami* originates with the Japanese meaning for folding (*ori*) of paper (*kami*); a traditional form of art where a single sheet of paper is transformed into different geometries based on the arrangement of fold-lines. Combining the art of origami with mathematical principles has led to origami science, which has been a key source of inspiration for scientist.
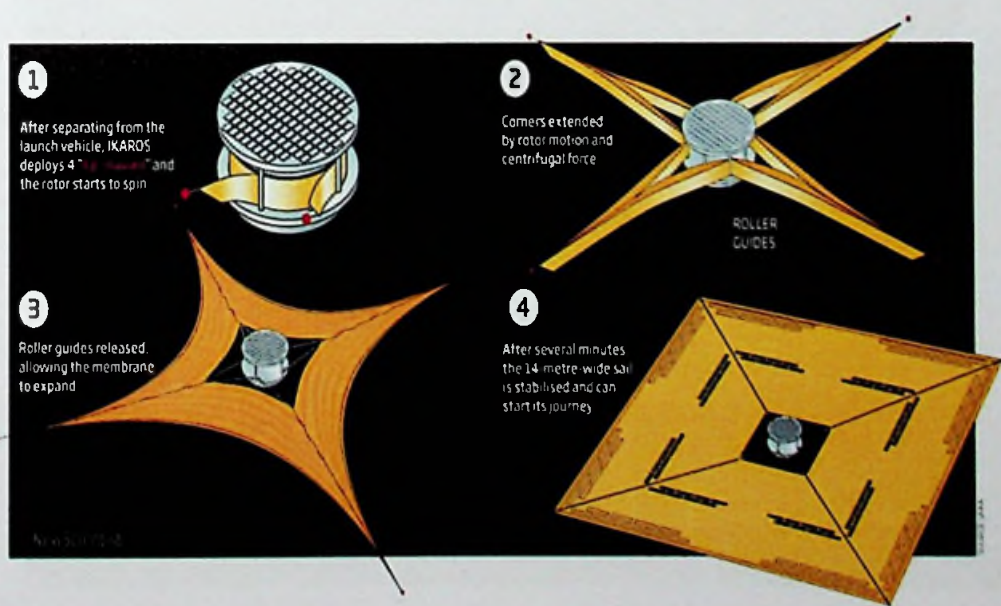
Figure 1.1: Deployment of IKAROS solar sail demonstrator (JAXA)

Miura (1989) introduced a novel folding pattern known as *Miura-Ori* pattern where the fold-lines are aligned at a specific angle allowing a large sheet to be easily folded with a simple linear motion (Figure 1.3). Large maps folded according to this technique can easily be viewed and then be stowed back making them ideal for travellers.

Based on origami science, Guest (1994) proposed a mathematical relationship to derive a wrapping pattern based on the polygonal shape. This pattern allows a single membrane to be wrapped around the central hub which will provide a higher stability in deployed state (compared to a membrane made by attaching small portions).

Modifying the fold-line alignment has led to different folding patterns with simplified deploying sequence. Figure 1.4 (a) and (b) compares the same geometry
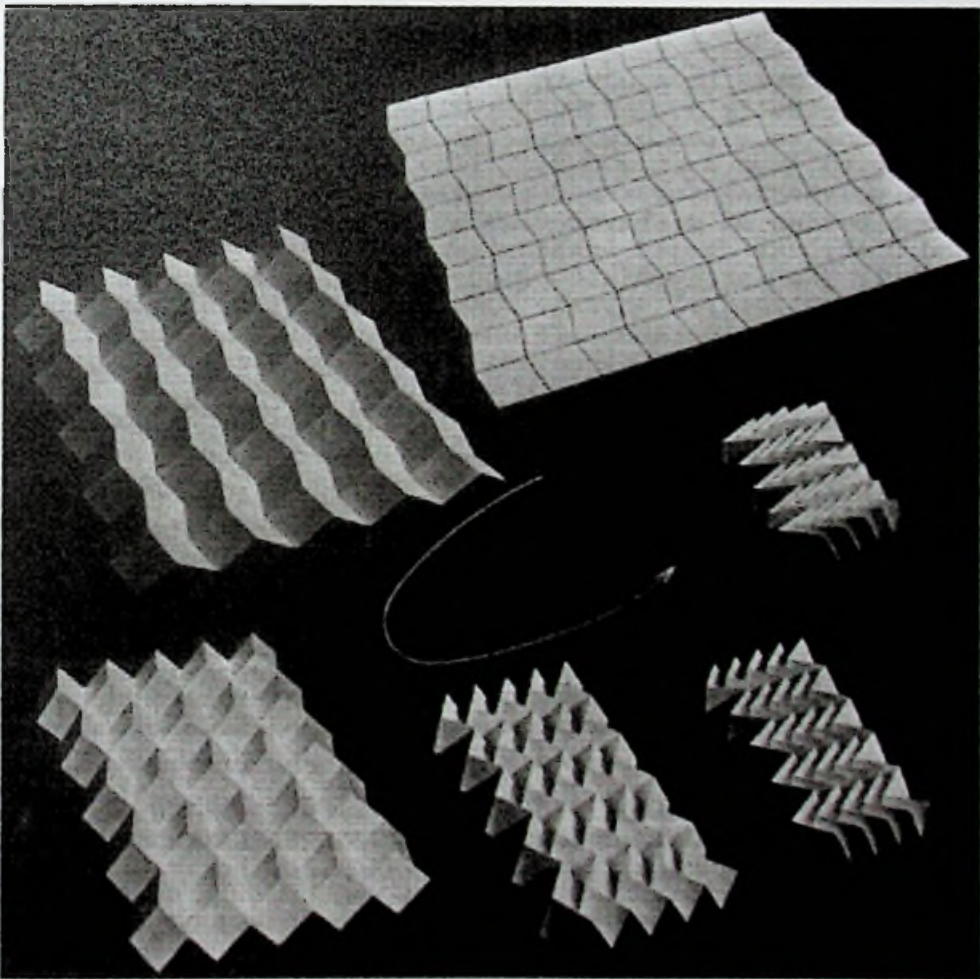
Figure 1.3: Miura folding pattern (Miura, 1989)

with spiral and circumferential folding patterns (Natori, Sakamoto, Katsumata, Yamakawa, & Kishimoto, 2014). Tessellation patterns can also be formed by repeating the same polygonal unit cells forming a large surface (Figure 1.4 (c)).

Expandable tubular shells are also used as a structural element for space structures. Guest (1994) describes about foldable cylinders with triangulated formations. Natori et al. (2014) have achieved trapezoidal formations by modifying the fold arrangements (Figure 1.5). The compaction and deployment of the tubular structure depends on the defined geometric formation while the compression capacity of each tube is likely to vary with the fold configuration.

1.2. Advanced Shell Structures

Apart from the ability to deploy from a compact state, thin folded membranes are getting popular among scientists for its unique features. Miura-Ori (Figure 1.3) and egg-box formation (Figure 1.6) patterns have significantly changed the global properties of the sheet due to fold-lines (Schenk, 2011). These properties can be used for structures that needs to endure amplified deformations without failure.

NASA's novel concept for a cooling radiator consist of Miura-Ori configuration allowing the radiator to expand or contract depending on the external temperature (Goddard Space Flight Center, 2017)

(a)

(b)

(c)
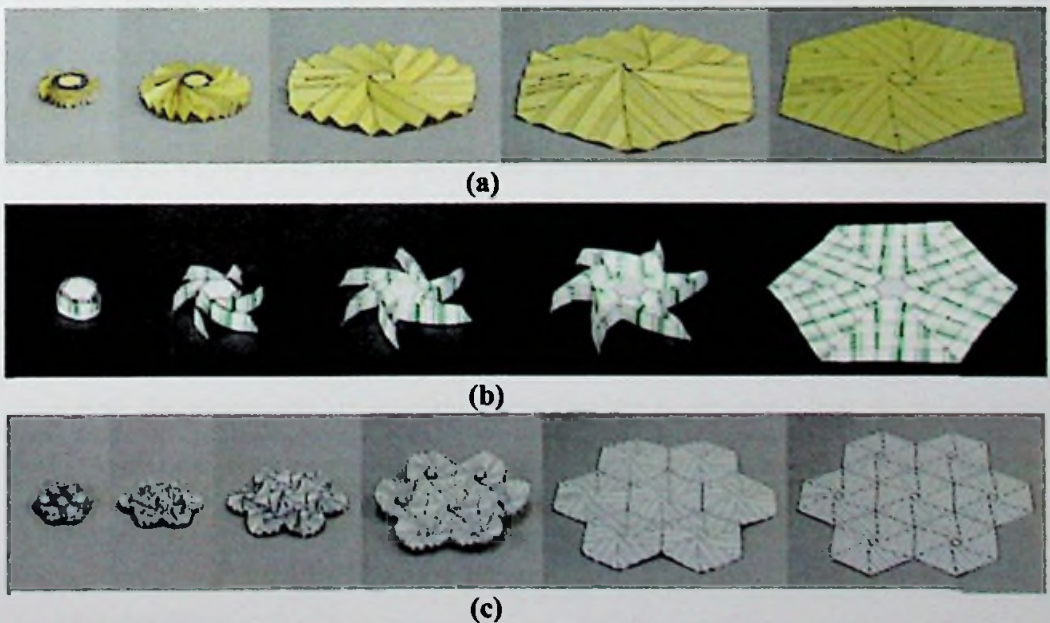
Figure 1.4: (a) Spiral Folding pattern, (b) Circumferential folding pattern and (c) Tessellation patterns (Natori, Sakamoto, Katsumata, Yamakawa, & Kishimoto, 2014)
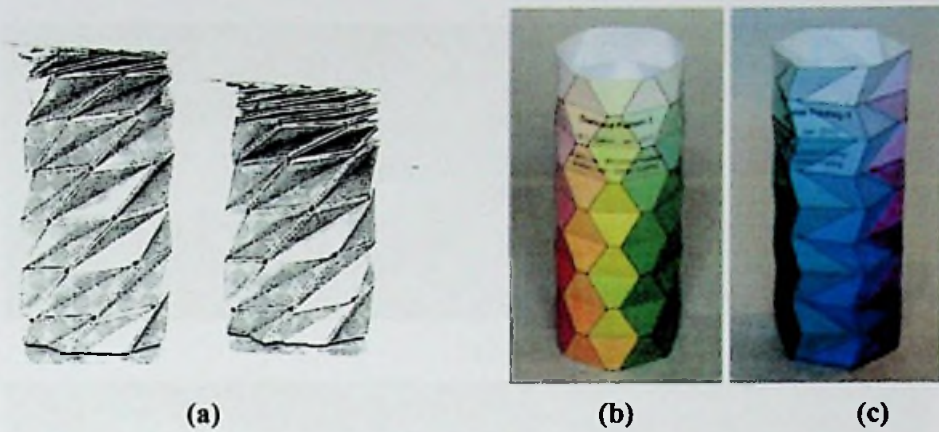
Figure 1.5: Foldable Cylinders

(a) Trianguated cylinders (Guest, 1994), (b) Trapezoid cylinder and (c) Slanted trapezoid cylinders (Natori, Sakamoto, Katsumata, Yamakawa, & Kishimoto, 2014)

The applications of foldable membranes have been applied in micron scale to develop new materials that exhibit unique features. Foldable meta-materials have the ability to expand by changing the geometric shape (Figure 1.7) and reconfigurable geometrics can change the material properties such as stiffness and strength (Overvelde, Weaver, Hoberman, & Bertoldi, 2017).

1.3. Testing in Virtual Environments

Product optimization of deployable membrane structures discussed previously is a demanding task due to their complex nature. Furthermore, these structures are likely to encounter extra-terrestrial environment conditions where the gravity, air resistance and temperature are different. Replicating the environmental conditions is one of the major constraints faced during the design phase. Parabolic flight path can attain gravity-less condition for a small time-span of about 20 seconds where a scaled physical model can to be tested. Pumping the air out from large vacuum chambers can reduce the air drag for testing, but can be a costly and time consuming alternate.

Rapid developments in computer technologies in past few decades have resulted in high quality processors with the ability to handle millions of computations per second. Finite element based software have since become a popular tool for engineers designing complex structures. Ability to change the environmental
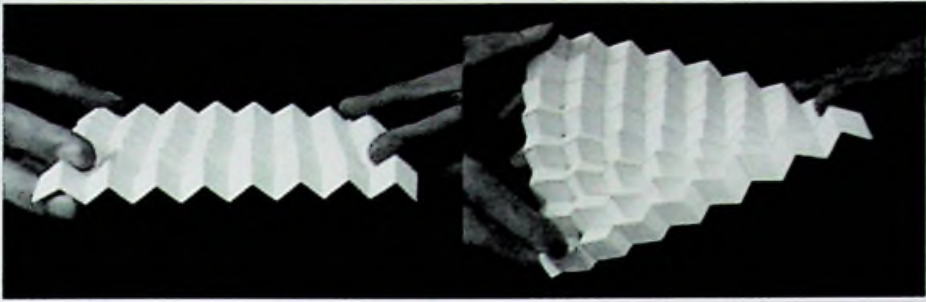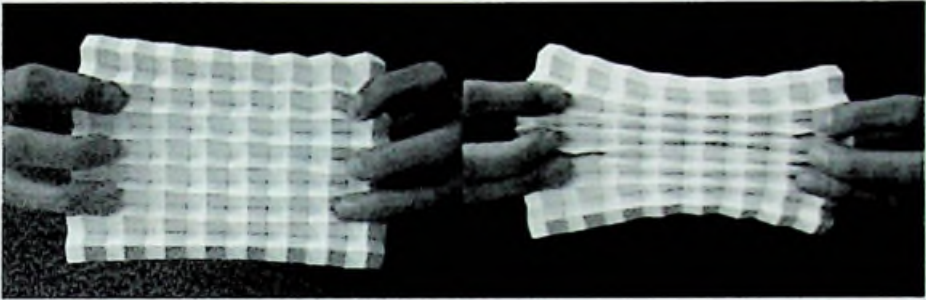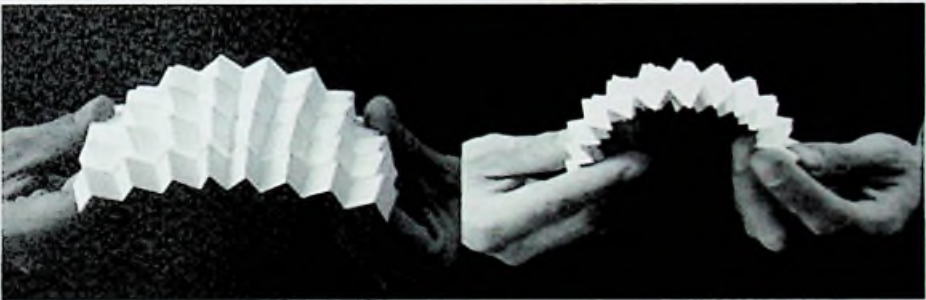
Figure 1.6: Flexibility of egg-box formation

(a) Twisting, (b) axial deformation and (c) bending (Schenk, 2011)

parameters with a simple command makes virtual simulations the best alternative when designing space structures.

Even-though by the outlook virtual simulations are deemed to be attractive, in depth validations need to be carried out to ensure that analysis is precise and considers the critical factors affecting the behaviour of the model.

Shirasawa et al (2011) has developed a spring-mass model where membrane is assumed to be isotropic and substituted by particles connected by springs and dampers. But damping of in-plane oscillations between main body and membrane needed to be improved. Sleight, et al. (2006) have developed separate virtual simulations for ground

6
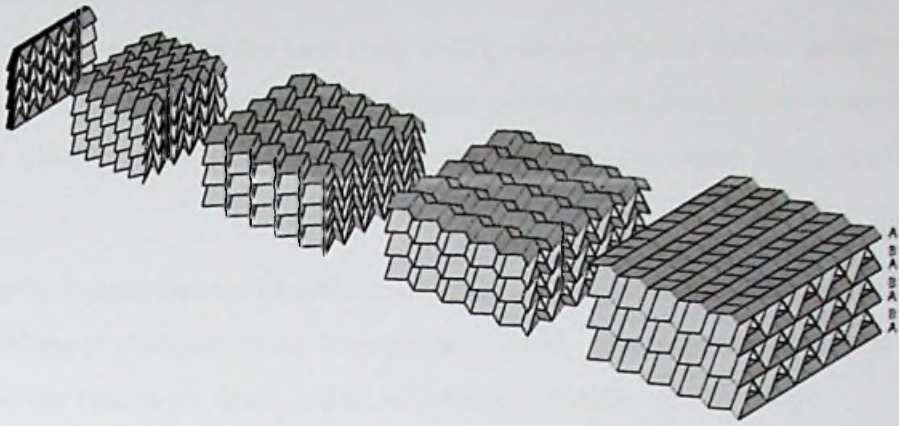
Figure 1.7: Foldable Meta-material (Source: Advance structures group, University of Cambridge)

deployment of a 10 m x 10 m sail by NASA. The ground simulation was in a vacuum chamber with gravity offloads. NEiNastran and ABAQUS software packages have been used for simulations. The analysis has provided results which are reasonably agreeing with the test data. Liyanage & Mallikarachchi (2013) have developed a simulation based on Abaqus commercial finite element software where spiral folding pattern and circumferential folding pattern were compared. They have further improved the model accounting for membrane thickness.

For simplicity, most of these simulations have neglected the effects arising from membrane folding. However, significance of fold-line behavior was highlighted by IKAROS solar sail demonstrator (Sakamoto, et al., 2014).

1.4. Scope and Aim

The aim of this research is to understand the mechanics of thin folded membranes and develop a suitable simulation technique with the capacity to accurately predict their behaviour. Hence the research focuses in the following sub objectives.

(i)   Characterizing the properties of a single fold using an experimental study and develop constitutive relationships

(ii)   Develop a simulation technique with the ability to incorporate fold-line behaviour.

(iii)   Validating the developed technique with an experimental case study.

7

1.5. Chapter Organization

Chapter 2 establishes the necessary background regarding folded membranes and investigates previous research work carried out to characterize their properties. Concept of neutral angle and the fold-line stiffness are discussed using previous literature.

Chapter 3 describes the experimental setup used to estimate fold-line stiffness for three different thicknesses of Kapton polyimide. The experimental data are analysed and the results are discussed to establish constitutive relationships.

Chapter 4 introduces a finite element simulation technique for a simple fold using Abaqus FEA (finite element analysis) software package. It further investigates the common issues in simulating shell structures and possible numerical errors.

Chapter 5 is focused on validating the developed technique using an experimental case study. Furthermore it compares several other idealization methods to identify the importance of incorporating fold-line stiffness.

Chapter 6 concludes the thesis with a discussion on the results and recommendations for future work.

CHAPTER II

2. FOLD-LINE PROPERTIES

This chapter focuses on identifying the parameters affecting the behaviour of folded membranes by investigating previous literature.

2.1. Geometric States of Folding

A crease or a fold-line can be defined as a residual mark on a membrane due to a previous folding action. Even though it appears to be a fairly simple concept, careful investigation is required to understand the behaviour of foldable structures..

Figure 2.1 exhibits the variation of geometric shapes of an A4 size sheet, (a) at its original state, (b) being fully folded at several locations and (c) new unstressed state after removing folding force. Parallel fold-lines have divided the original flat sheet into number of portions by changing the surface inclination of each portion.

If a similar load is applied to configurations before folding and after folding, they will be behaving in two separate approaches. If both are subjected to similar in-plane compressive forces (perpendicular to fold-lines), latter will compress by varying the angle between shell portions whereas the unaltered sheet will deform by bending at the middle region. If a force was applied parallel to fold-lines, the latter sheet would exhibit higher stiffness and resist the compressive force whereas the first sheet will behave same as before.

Wang, Tan, & He, (2010) have identified different stages of membrane creasing and unfolding. The initial stress free configuration is a flat sheet without any deformations and once the folding load is applied, stress free geometry alters by

<div align="center">(a)   (b)   (c)</div>
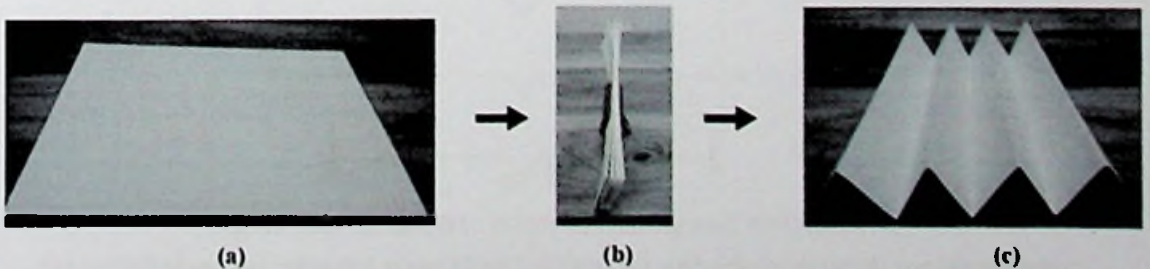
Figure 2.1: Geometric configuration of a paper sheet before and after introducing fold-lines (a) initial undeformed shape, (b) fully folded shape and (c) new unstressed shape

dividing the sheet into "V" shaped two portions with different face angles on either side of the fold. The internal angle formed between two shell portions (φ) will be defined as the angle of relaxation or the neutral angle (Figure 2.2). When an unfolding force is exerted, the membrane bends near the fold-line due to an internal resistive moment at the fold-line. Due to the kink shaped deformation, membrane cannot be fully unfolded and there will be residual stresses appearing in the membrane.

2.2. Deformation Profile at the Fold

One of the apparent modifications in the membrane is the deformation profile while unfolding. Lechenault, Thiria, & Adda-Bedia (2014) have identified two possible deformations in a membrane; (1) Membrane bending near the fold line and (2) Opening of the fold-angle (Figure 2.3). The final deformed shape is a resultant of membrane bending and fold opening while in some cases one method becomes dominative.

They have further established a relationship between bending energy and crease energy of a folded membrane to identify which method becomes dominative for the deformed shape. They introduced a term called characteristic length (L^*) where,

$$L^* = \frac{Bending\ energy\ of\ membrane}{Hinge\ energy\ of\ the\ fold} \tag{2.1}$$
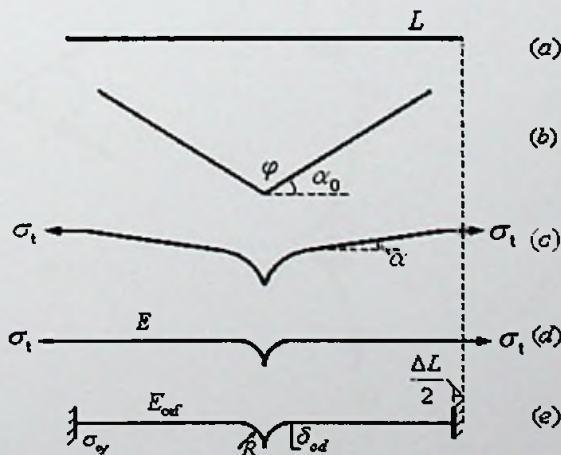
Figure 2.2: Geometric states of folding and unfolding
(a) Initial state (b) released state after folding, (c) unfolding state (d) tensile creased state (e) Baseline configuration with effective modulus and residual stresses from creasing (Wang, Tan, & He, 2010)

10

It was identified that if the length (l) between two folds is greater than L^*, then the membrane bending is dominative. If l is lesser than L^* fold opening is dominative. Figure 2.4 illustrates this concept where the first membrane is having high bending energy and therefore it is unfolding through the opening of fold angle. The bottom membrane in the figure is having a lower bending energy and therefore membrane is bending near the fold.

The bending stiffness of a membrane is dependent on material and section properties (i.e. Young's modulus, poisson's ratio, thickness) which is incorporated in finite element simulations through section definition. To obtain accurate output, crease energy should also be included separately.
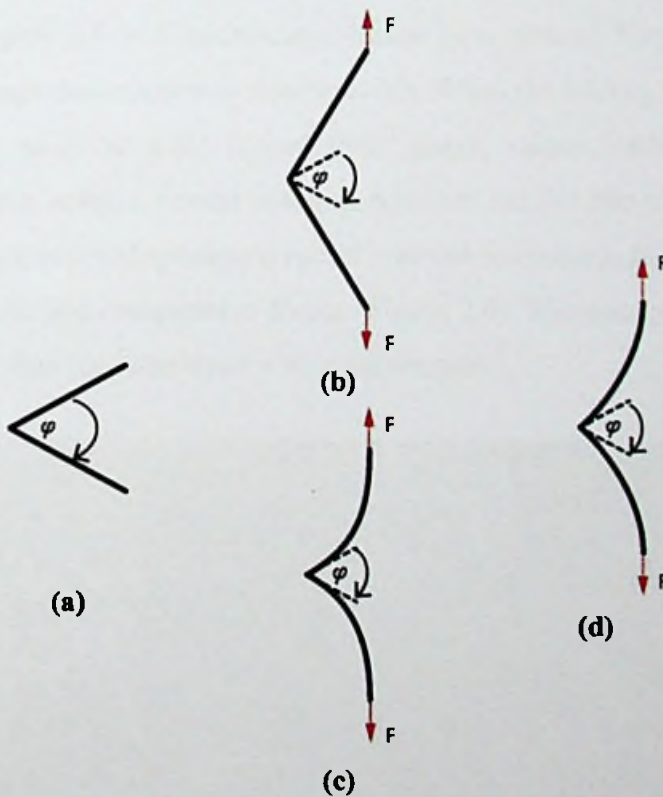
Figure 2.3: Deformation of a folded membrane, (a) unstressed state (b) fold-angle opening, (c) membrane bending and (d) actual deformation profile
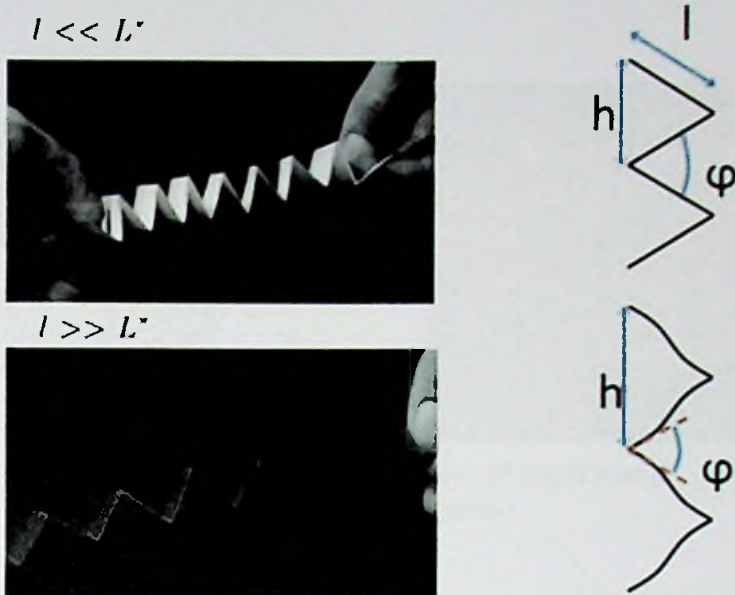
Figure 2.4: Characteristic length for deformed shape

2.3. Plastic Deformation of Material

Folded membranes have localized deformations in the material which modifies their properties. Figure 2.5 is a microscopic image of a creased Kapton specimen where the kinked shape deformation is clearly visible. When the folding load is applied membrane stresses near the kink exceed their elastic values leading to plastic deformations. Kapton being a ductile material does not exhibit the fractures in the material. However paperboard specimens reveal material fractures in the membrane at the fold due to tensile and compressive forces (Figure 2.6). Microscopic fractures in the material can weaken the membrane with a failure path.
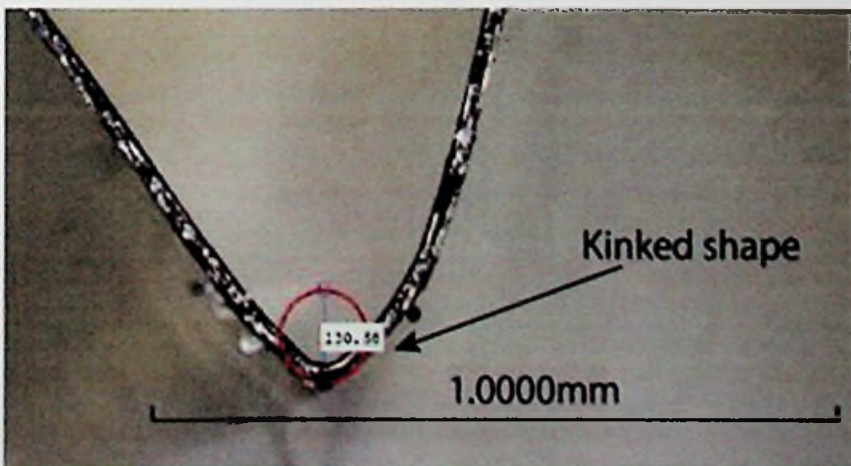
Figure 2.5: Kinked shape deformation of Kapton

12
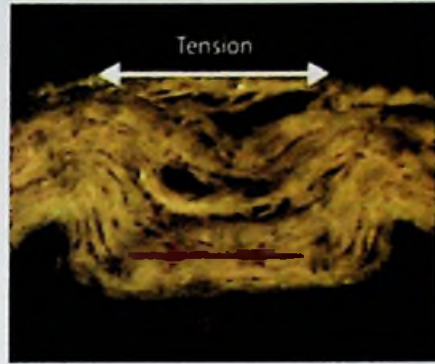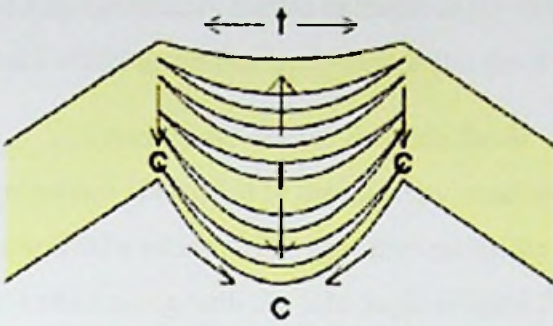
Figure 2.6: Microscopic deformations of paperboard
(Beex & Peerlings, 2009)

2.4. Fold Endurance Test

The folding endurance test measures a combination of tensile strength, stretch and fatigue properties of a folded membrane. The weakening of the material at the fold is assessed by checking the number of fold-unfold cycles it can endure with a tensile force applied. The test specimen is 15 mm wide and at least 125 mm long with clean cut edges.

The specimen is clamped between the oscillating head and the stationary head. Tensile force resulting from 1 kg mass is applied on the membrane and the oscillating head is rotated at 175 ± 25 folds per minute. Number of double folds are recorded until failure (Figure 2.7).
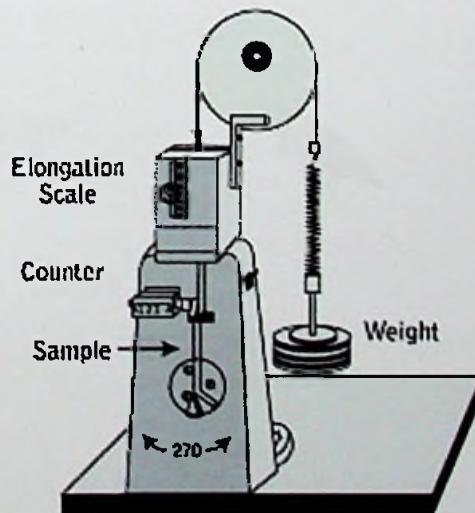
Figure 2.7: MIT Fold Endurance tester

2.5. Hinge Response at the Fold

Folding not only alters the geometric properties, but the mechanical properties of a membrane. A classic example is the origami frog which can jump due to spring-back effect generated by folding a flat sheet of paper.

Lechenault, Thiria, & Adda-Bedia (2014) have investigated the mechanical properties of a folded Mylar sheet by attaching two force sensor at its edges. They have identified a resistive moment preventing the fold from freely opening and plotted the variation along with the fold-angle (Figure 2.9). It can be observed that the fold angle corresponding to zero resistive moment is around 50° degrees which is the angle of relaxation/neutral angle. Opening or closing of the neutral angle is resisted with an internal moment varying from negative to positive. The relationship between moment (M) and current fold angle (θ) can be interpreted as

$$M = k\,(\theta - \varphi) \tag{2.2}$$

where φ is the neutral angle and k is the gradient of the graph.

Yasuda et al. (2013) have investigated the behaviour of a fold by applying a compression force and developed an experimental relationship. Strathmore 500 Bristol, 2 Ply paper sheets with a thickness of 270 µm was used for the experiment and the forces were measured through IMADA DS2 – 1 Digital Force Gauge. A graph was plotted between resistive moment (M) and folding ratio (θ^*), which is a non-
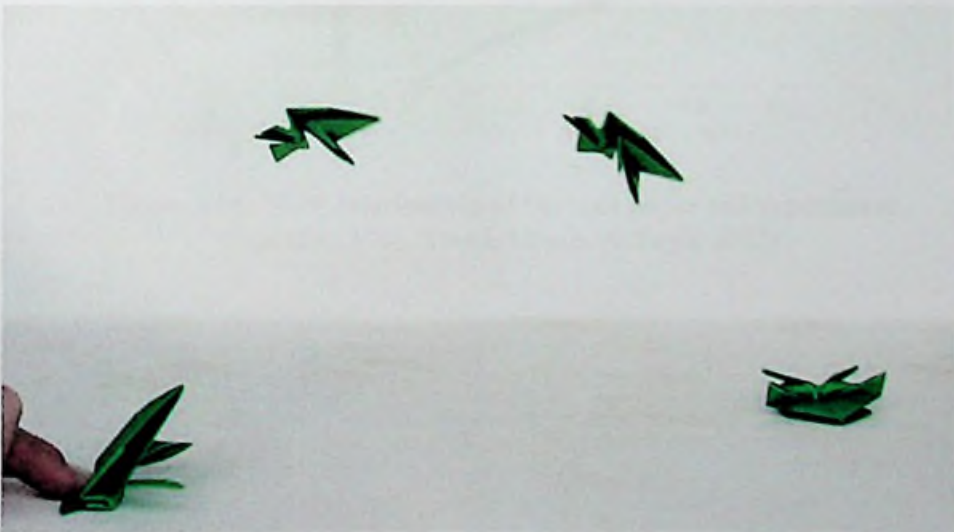
Figure 2.8: Jumping Origami frog (Baldwin, 2015)
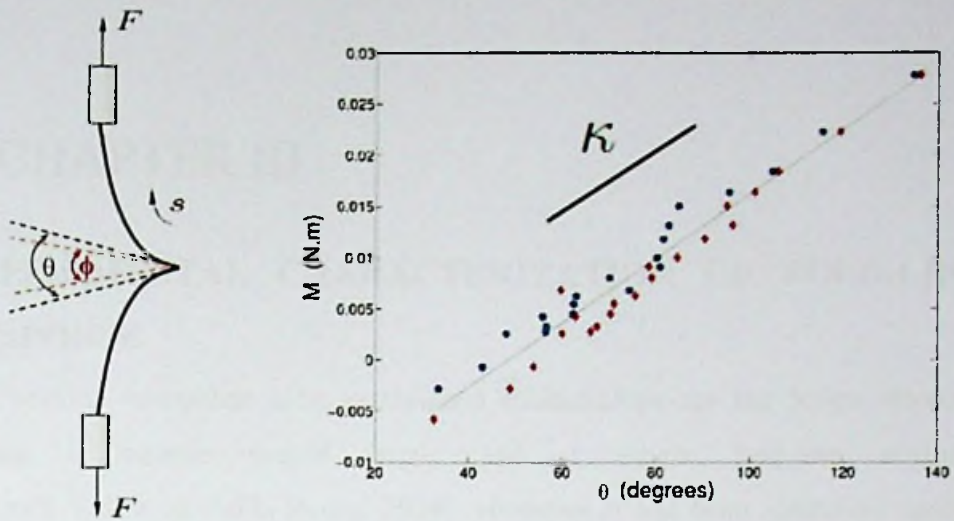
Figure 2.9: Moment angle relationship for Mylar 350 μm (Lechenault, Thiria, & Adda-Bedia, 2014)

dimensional unit defined as $\theta^* = \frac{\varphi - \theta}{\frac{\pi}{2} - \varphi}$ where θ is the current angle and φ is the initial

(neutral) angle as measured in Figure 2.10. The resistive moment is increased linearly while the fold-angle closes due to compressive load and after reaching a folding ratio of 80%, a sudden stiffness increase is observed.
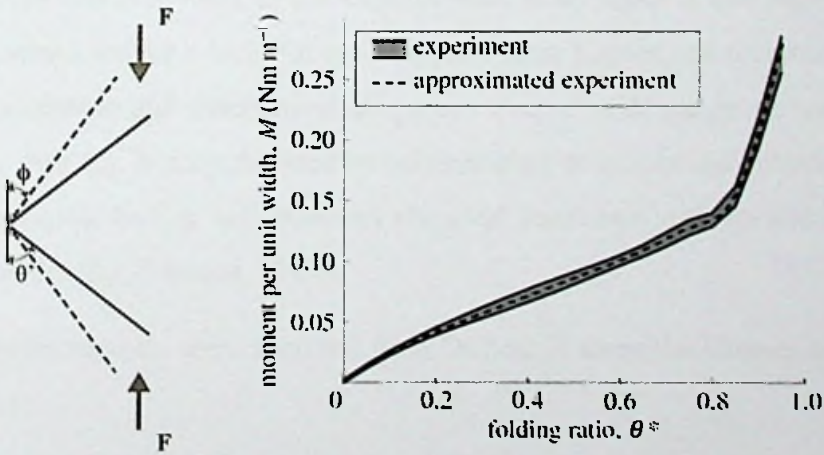
Figure 2.10: M–θ* relationship of the unit paper cell experiment (Yasuda , Yein, Tachi, Miura, & Taya, 2013)

CHAPTER III

3. EXPERIMENTAL CHARACTERIZATION OF FOLD-LINE RESPONSE

Previous researches have established relationships for the hinge response specifying a unique neutral angle and a single fold-line stiffness (Lechenault, Thiria, & Adda-Bedia, 2014). However it has been identified neutral angle is dependent on many factors including method of creasing, level of scouring and applied folding pressure (Abbott, 2014). Figure 3.1 shows three instances of 300HN Kapton samples with different neutral angles obtained by varying the applied pressure.

The objective of this experiment is to capture the variation of hinge response and develop a reliable relationship that can estimate the fold-line stiffness accurately. Kapton polyimide was used in the experimental setup since it has high durability properties which makes it ideal for space applications. Kapton can maintain excellent physical, electrical and mechanical properties over a wide range of temperatures (-269° C to 400° C). It is synthesized by polymerizing an aromatic dianhydride and an aromatic diamine, having and excellent chemical resistance with no known organic solvents for the film (Dupont, 2017).

Kapton samples were acquired from DuPont in three thicknesses as indicated in Table 3.1.
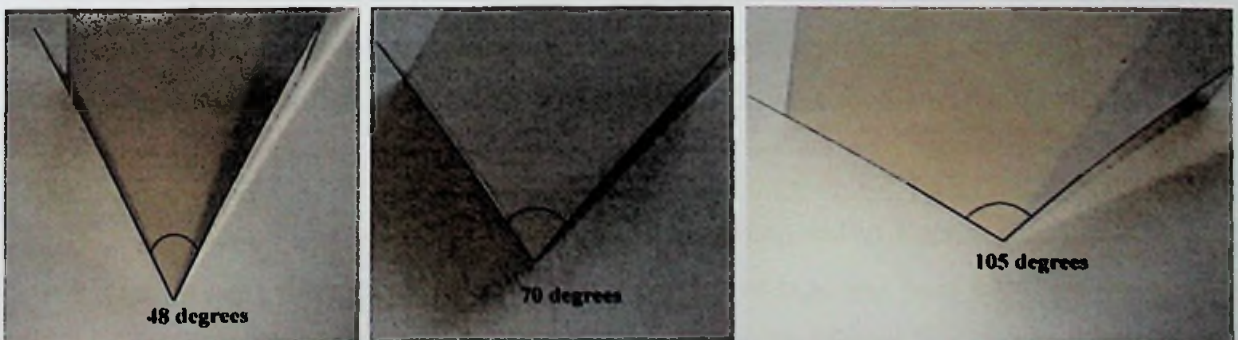
Figure 3.1: Variation of neutral angle to folding method

Table 3.1: Material Properties of Kapton samples (Dupont, 2017)

	Units	100 HN	200 HN	300 HN
Thickness	μm	25	50	75
Density	kg/m³	1420	1420	1420
Ultimate tensile strength	MPa	231	231	231
Tensile Modulus	GPa	2.5	2.5	2.5
Poisson's ratio		0.34	0.34	0.34
MIT folding endurance	cycles	285 000	55 000	6 000

3.1. Experimental Setup

Since our primary focus is to identify the variation of resistive moment for different fold angles, it is imperative that dominating deformation mechanism should be fold-opening rather than membrane bending. Hence length of the membrane needs to be restricted to a minimum (L^*). It was decided to size the specimen to a length of 40 mm with the fold located at its middle. Further reducing the length will encounter additional problems with handling the specimen and attaching loads. After few trial and error iterations the width was selected to be 20 mm, where wider specimens experienced non uniform fold opening and narrow specimens had large deformations due to reduced moment carrying capacity.

The Kapton sheet was marked into 20 mm x 40 mm rectangles and then cut using a sharp blade with clean edges. The membrane was bent symmetrically by keeping its two edges on top of each other and then the roller was carefully passed over the membrane with uniform intensity. The number of roller passes were varied between different specimens to obtain different neutral angles. After applying the folding pressure, specimens were kept undisturbed for 2 hours for them to self-open to the neutral angle, Figure 3.2.

A timber frame with relatively high rigidity compared to Kapton membrane was used to hang the specimen. Low stiffness adhesive tape was used to attach the specimen to the timber frame to minimize the moments transferred from the support.

(a) Marking
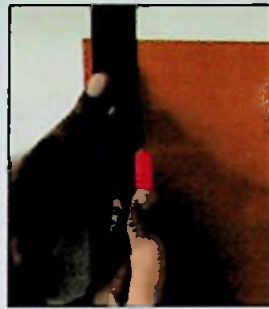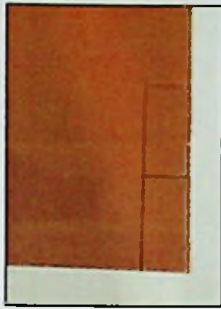
(b) Cutting
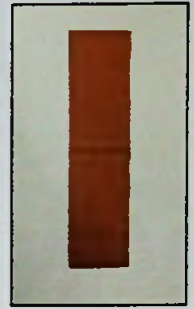
(c) Folding
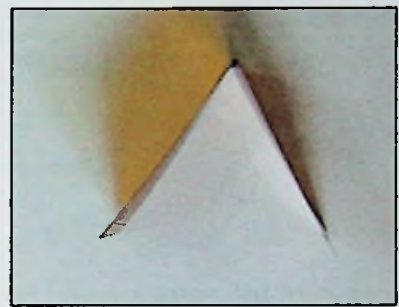
(d) Final unstressed configuration

Figure 3.2: Preparation of test specimen

Though attaching a rigid strip distributes the unfolding load uniformly it adds a significant weight component. Hence a nylon string was connected to the mid-point of the bottom edge allowing the gravitational load to impose a symmetric in plane unfolding force (Figure 3.3). No wrinkles were observed during the experiment. A combination of beads weighing 0.10 g, 0.61 g and 2.1 g were attached to the string for loading.

The experiment was carried out in a closed environment to minimize the effects of wind and vibrations. The loads were applied stepwise, and after each step the specimen was left undisturbed to obtain static equilibrium. A digital camera (20 megapixel) was used to capture the equilibrium state as shown in Figure 3.4. Captured images were processed using WebPlotDigitize tool to measure angles, θ and distances, x. The calibration grid visible in the background was used to convert pixels to millimetres. Angle measurements were carried out by drawing tangents to the
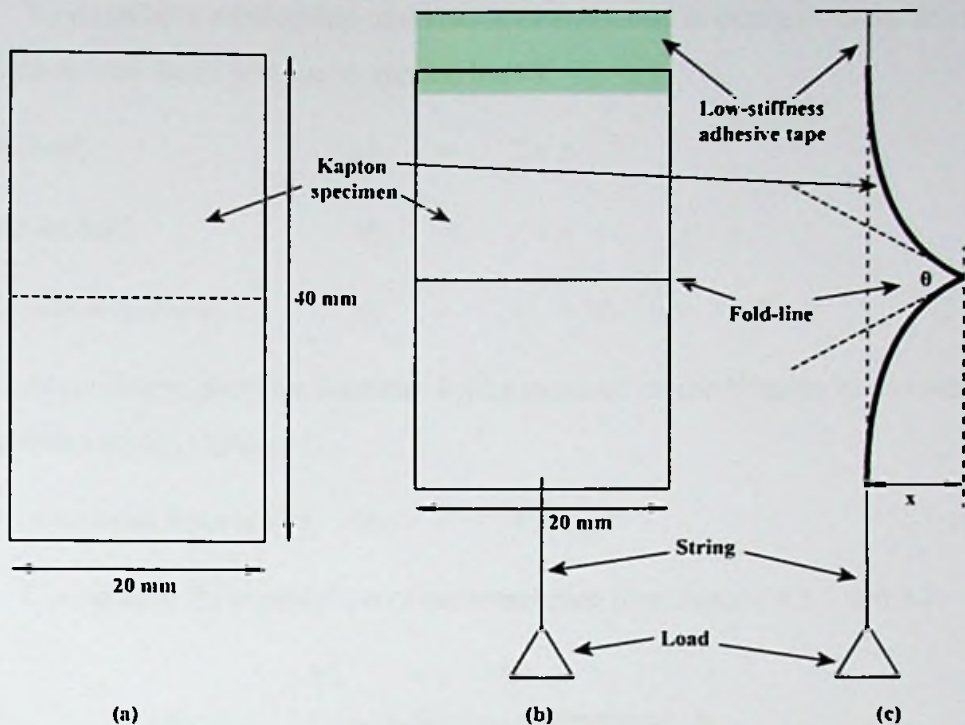
Figure 3.3: Schematics of the membrane specimen (a) before folding, (b) front view and (c) side view of the folded membrane with boundary conditions

specimen at the kinked edge. The experiment was conducted for 16 specimens with different thicknesses and neutral angles, as indicated in Table 3.2.

Table 3.2: Specimen details

	Test	1	2	3	4	5	6
100HN	Neutral angle	37°	50°	73°	77°	91°	110°
200HN	Test	7	8	9	10		
	Neutral angle	36°	45°	74°	88°		
300HN	Test	11	12	13	14	15	16
	Neutral angle	42°	43°	76°	86°	107°	114°

3.2. Moment – Angle relationship

Let's consider a pre-folded membrane having a neutral angle of φ, with pinned boundary conditions. When an in-plane tensile force T is applied to the membrane it will increase the fold angle to θ while aligning the crease at x distance from the boundaries (Figure 3.5).

To establish a relationship of resistive moment due to external forces M_e, take moments around the crease due to applied load T,

For top half, M_1 = $T \times x$

For bottom half, M_2 = $T \times x$

Total external moment, M_e = $M_1 + M_2$ $= 2 \times T \times x$ (3.1)

According to previous literature it was assumed crease behaves as a rotational spring with a spring stiffness k.

Resistive moment from crease, M_r = $k (\theta - \varphi)$ (3.2)

Considering the equilibrium of the membrane from equation 3.1 and 3.2,

$$M_e = M_r$$

(a)

(b)
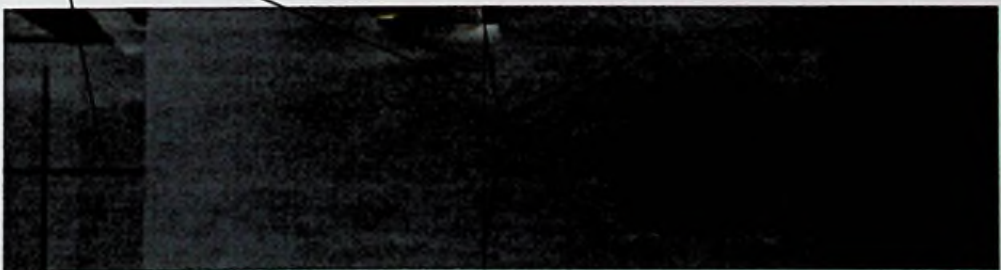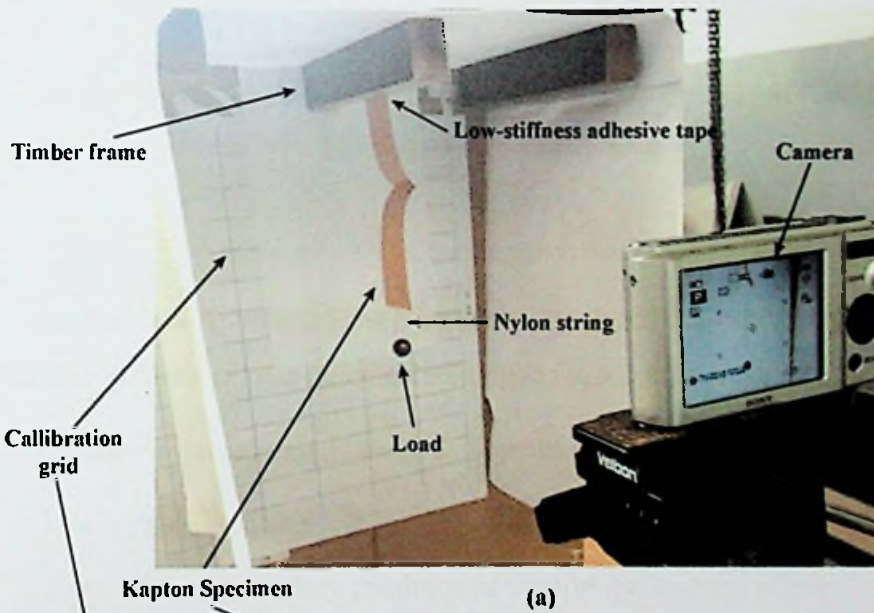
Figure 3.4: (a) Experimental setup and (b) image captured for
digital image processing

20
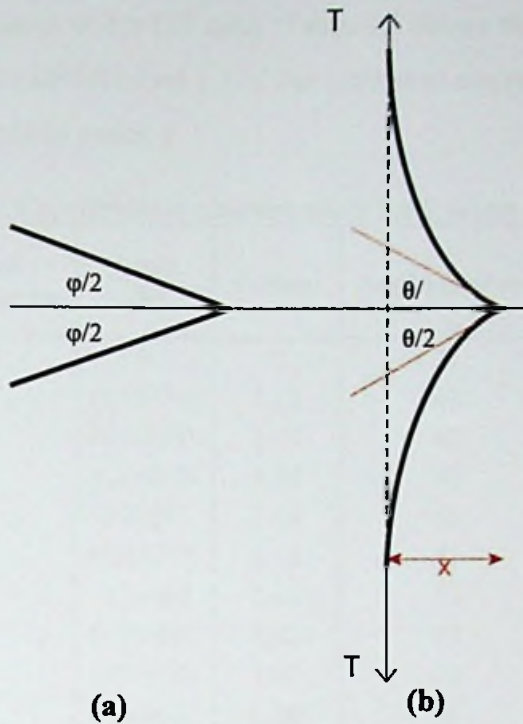
Figure 3.5: Moment angle relationship
(a) Neutral angle φ at unstressed state and (b) opening of fold angle to θ
due to membrane force T

$$M \quad = \quad 2 \times T \times x \quad = k\,(\theta - \varphi) \tag{3.3}$$

Applied load T is varied and x and θ are measured. By plotting the $M - \theta$ graph the fold-line stiffness (k) can be calculated by the gradient.

The above formulation is subjected to following assumptions.

- The self-weight of the membrane is negligible
- Pinned boundary condition at the top and bottom edges
- Fold-angle is uniform with constant resistive moment being applied to the membrane

3.3. Results

The deformation profile of a 200HN specimen is shown in Figure 3.6 when the load is gradually increased. The kinked shape deformation is clearly visible which prevents the membrane from fully unfolding. Measured angles and distances are processed according to Eq. 3.3 to estimate the resistive moments which are then

divided by the specimen width (20 mm). Table 3.3 shows the angle (θ) and distance (x) measurements for 100HN Test 1 and the estimated resistive moments. Details of other tests are attached in annex 1.

Table 3.3: Experimental measurements for Kapton 100HN Test 1

Membrane	Test Specimen	Load (N)	x (mm)	Angle(degrees)	Moment per unit length (Nmm/mm)
100HN	1	0		37	0
		0.000981	8.12	41	0.0008
		0.002943	5.89	42	0.0017
		0.004905	4.96	43	0.0024
		0.00981	3.69	48	0.0036
		0.014715	3.14	51	0.0046
		0.01962	2.63	58	0.0052
		0.031981	2.02	63	0.0065
		0.044341	1.63	70	0.0072
		0.069062	1.26	74	0.0087
		0.093784	0.99	78	0.0093

Separate moment – angle plots were developed for each thickness (Figure 3.7, Figure 3.8 & Figure 3.9). Similar to Figure 2.9, linear relationships are established between resistive moment and fold-opening. The slope is very similar between different samples, indicating that the stiffness (k) of the fold does not depend on the particular neutral angle. This is further emphasized in Figure 3.10, which compares the results from all three sets of experiments, showing that they can be approximated by three different values of the linear bending stiffness of the fold, one
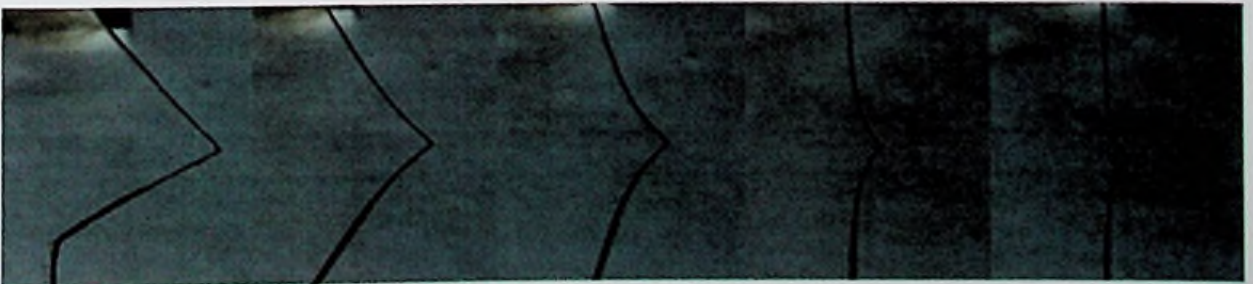
Figure 3.6: Deformation profile of Kapton 200 HN

22

for each thickness. The values of the best fit and their R^2 values, obtained by regression analysis, are presented in Table 3.4.

Table 3.4: Summary of Regression analysis

	100 HN	200 HN	300 HN
Membrane thickness (μm)	25	50	75
R^2 (%)	92.7	96.23	91.82
Gradient	0.0003	0.0012	0.0051

Hence the fold-line stiffness of the membrane is dependent on the neutral angle and following relationship can be used to predict the resistive moment generated..

$$Moment = k \; x \; (fold \; angle - neutral \; angle)$$

For 100 HN $\qquad M = 0.0003 \, (\theta - \phi)$ $\qquad\qquad$ (3.4)

For 200 HN $\qquad M = 0.0012 \, (\theta - \phi)$ $\qquad\qquad$ (3.5)

For 300 HN $\qquad M = 0.0051 \, (\theta - \phi)$ $\qquad\qquad$ (3.6)

where angles are in degrees and Moments are in Nmm/mm
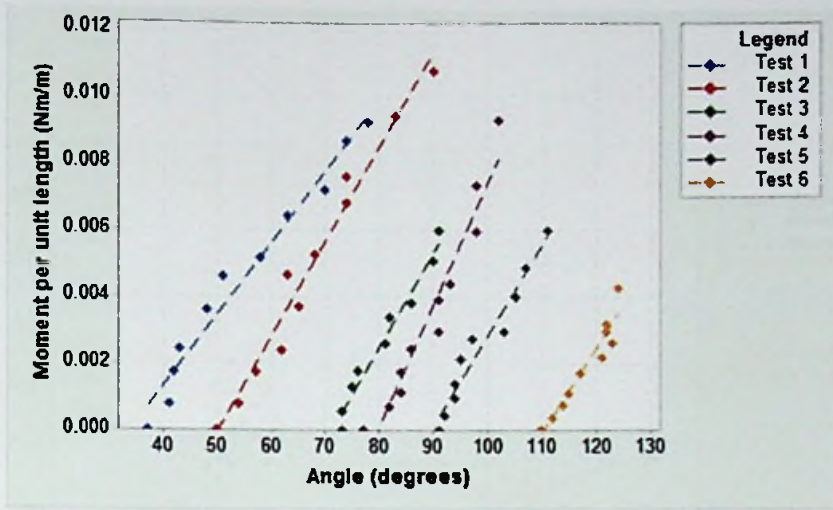
Figure 3.7: Moment - angle relationship for Kapton 100HN (25 µm)
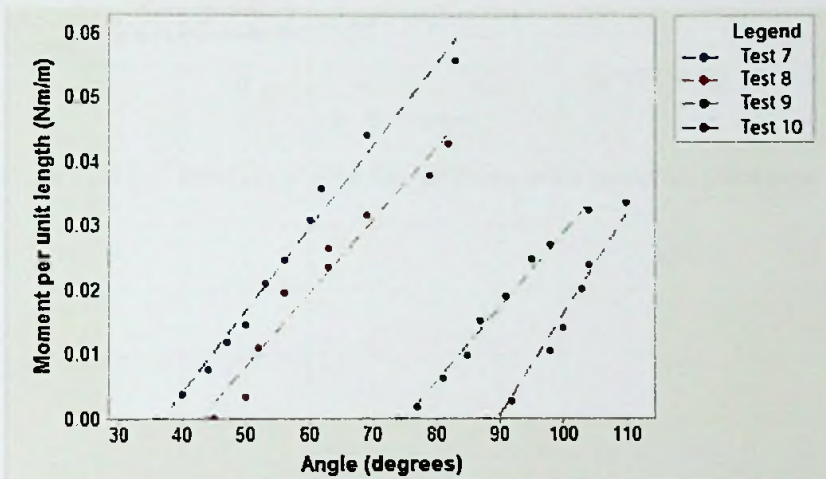
Figure 3.8: Moment - angle relationship for Kapton 200HN (50 µm)
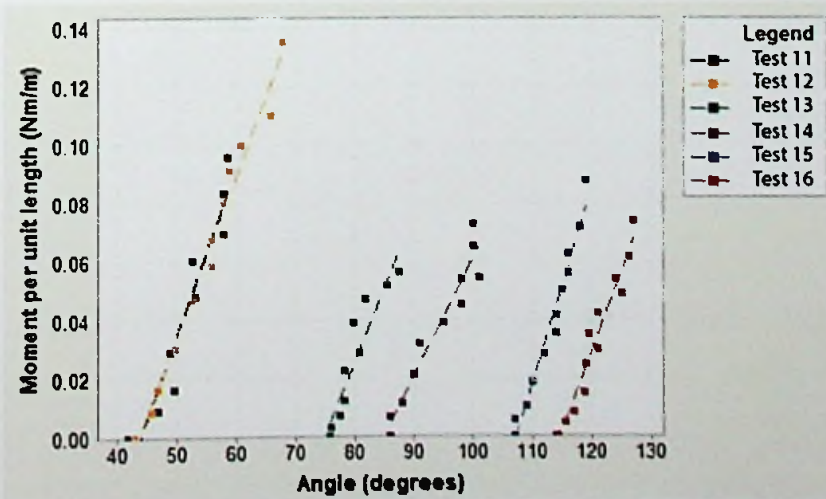
Figure 3.9: Moment - angle relationship for Kapton 300HN (75 µm)
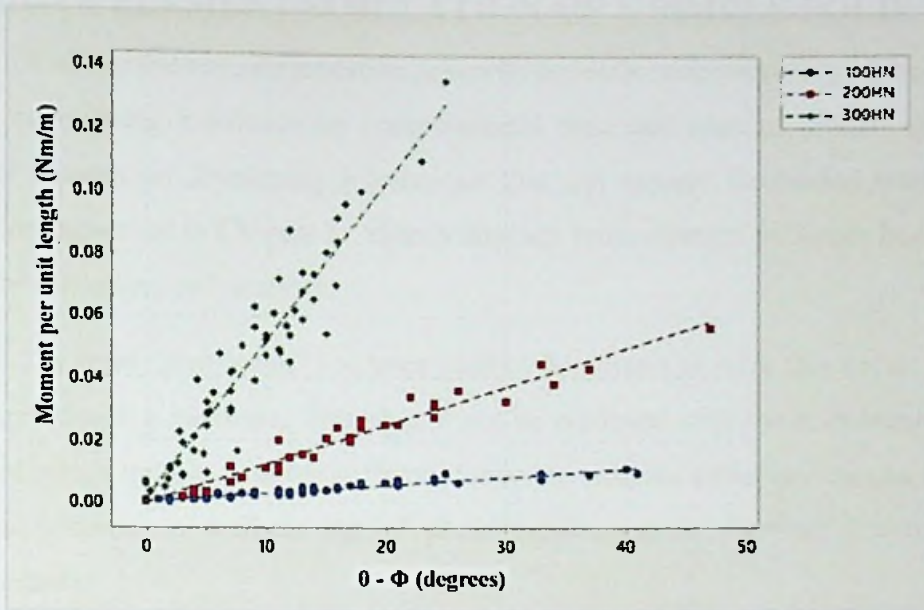
Figure 3.10: Variation of fold line stiffness with material thickness

CHAPTER IV

4. FINITE ELEMENT SIMULATION OF A SIMPLE FOLD

A successful virtual simulation primarily depends on the accuracy of the output while maintaining a balance on computational time and ease of modelling. This chapter focuses on developing a technique that can capture the folded membrane behaviour observed in Chapter 3. Abaqus/Explicit finite element packages have been used for modelling and analysis.

The term "membrane" has been used in this thesis to refer thin sheets which can carry bending moments. This should not be confused with the membrane finite element which ignores bending stiffness. Since the sections under review can handle in-plane stresses as well as out of plane bending, shell elements are used in idealizations.

In order to assess the suitability of idealization method and other simulation parameters, a single fold specimen used in above experiment was simulated. The specimen was 20 mm wide and 40 mm long with a fold-line at the middle. Kapton material properties are indicated in Table 3.1.

4.1. Modelling of Thin Shells

Folded membrane was modelled with two separate shell portions of 20 mm x 20 mm and fold-line properties were defined using the connection mechanism between them. Micro-scale plastic deformations (Figure 2.5) can be neglected since the membrane is discontinuous. The initial configuration was set to be at fully folded state (0° opening angle) with one edge pinned and other was smoothly displaced to simulate deployment process (Figure 4.1).

Abaqus/Explicit element library consists of number of shell elements that can be used for thin walled structures. The element formulation mechanisms are different from each other and their suitability was assessed considering accuracy and computational time. Following readily available conventional shell elements were considered in the comparison.
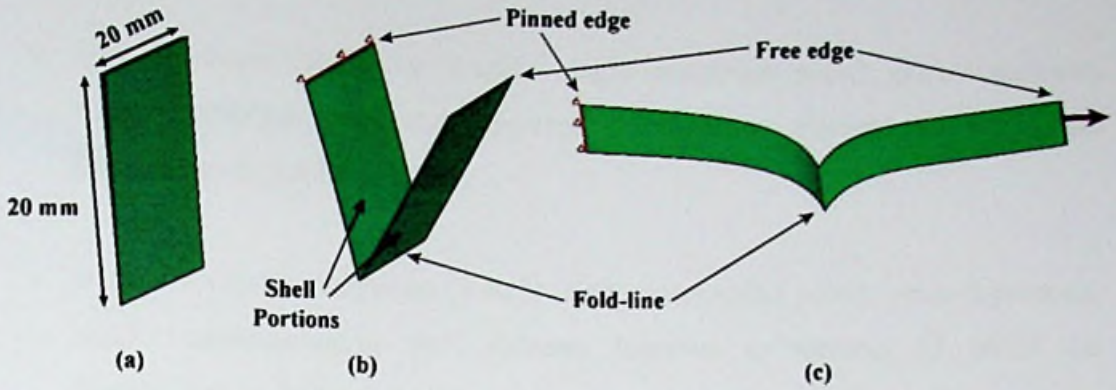
Figure 4.1: Finite element model for a single fold
(a) folded configuration, (b) self-opening to neutral angle* and (c) unfolded state
(* only when idealized as a rotational spring)

- S4 - Element type S4 is a fully integrated, general-purpose, finite-membrane-strain shell element. The element's membrane response is treated with an assumed strain formulation that gives accurate solutions to in-plane bending problems. It is not sensitive to element distortion, and avoids parasitic (shear) locking.

    Element type S4 does not have hourglass modes in either the membrane or bending response of the element and the element does not require hourglass control. The element has four integration locations per element compared with one integration location for S4R, which makes the element computationally more expensive.

- S4R - Reduced integration (4 node- single integration point), general-purpose, finite membrane-strain shell element. An efficient quadrilateral shell element with a single integration point; however, it can perform poorly when warped.

- S4R(h) - Reduced integration (4 node- single integration point), general-purpose, finite membrane-strain shell element (similar to S4R) with enhanced hourglass control.

- S4RSW - Reduced integration(4 node- single integration point), shell element with hourglass control, small membrane strains, warping considered in small-strain formulation

- S3R - Reduced integration (3 node- single integration point), general-purpose, finite membrane-strain shell element. Identical to element S3 while the formulation is similar to S4R

- S3RS - Reduced integration (3 node- single integration point), general-purpose, small membrane-strain shell element. Identical to element S3 while the formulation is similar to S4RS

Abaqus/Explicit only supports linear shell elements which will be poor in capturing bending curvatures. Hence the regions undergoing high curvatures need to be finely meshed to attain the correct deformation shape (Figure 4.2).
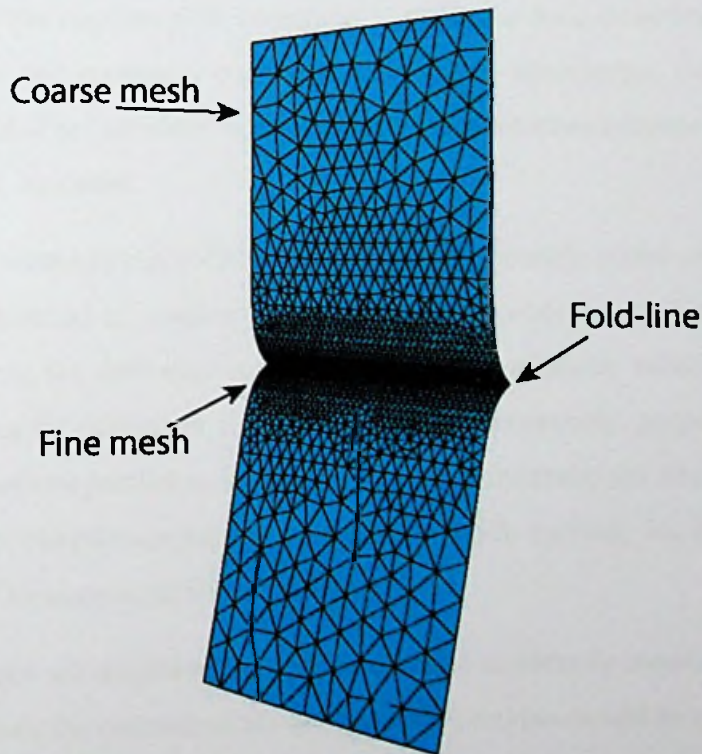
Figure 4.2: Mesh pattern to capture high curvature around fold-line

4.2. Modelling of the Fold-line

Three main idealization approaches were followed.

(i)   Minimum hinge energy: connection is assumed to be a perfect hinge with no restraints.

(ii)   Maximum hinge energy: connection is assumed to be a perfect weld which does not allow the fold-angle to change.

(iii)   Modified hinge energy: connection is assumed to be a rotational spring which can be modified by the user

Perfect hinge condition was modelled using a tie constraint between the two edges without fixing the rotational degrees of freedom. Weld condition was modelled using a tie constraint with rotational fixities. Both of these methods are simple and easy to incorporate into a complex structure. The third method is to define a special connector with rotational elasticity between the membranes.

4.2.1. Node to Node Connectors with Rotational Elasticity

This technique requires a tie constraint to maintain the connectivity between two shell portions and rotational connector elements to incorporate the rotational elasticity at the fold. The "revolute" connector which has rotational degree of freedom around local axis 1 was used.

Connector elements can only be defined between specific nodes and therefore the shell was partitioned to number of portions. Nodes were selected to represent similar lengths along the shell edge making the rotational elasticity value a constant. The connectors can be defined in two configurations; connectors' perpendicular to fold-line and connectors parallel to fold-line. Figure 4.3 illustrates the arrangement of connectors in two distinct connecting methods. In both methods local axis 1 of connectors should be aligned parallel to the fold.

Two portions are displaced by a small distance to identify connecting nodes from each edge. Once the connectors are defined shell portions should be re aligned to their original position to make the membrane continuous. Further, this will align diagonal connectors in Figure 4.3 (b) parallel to the fold. But in Figure 4.3 (a) two nodes will overlap and the connector will disappear once the gap in between is
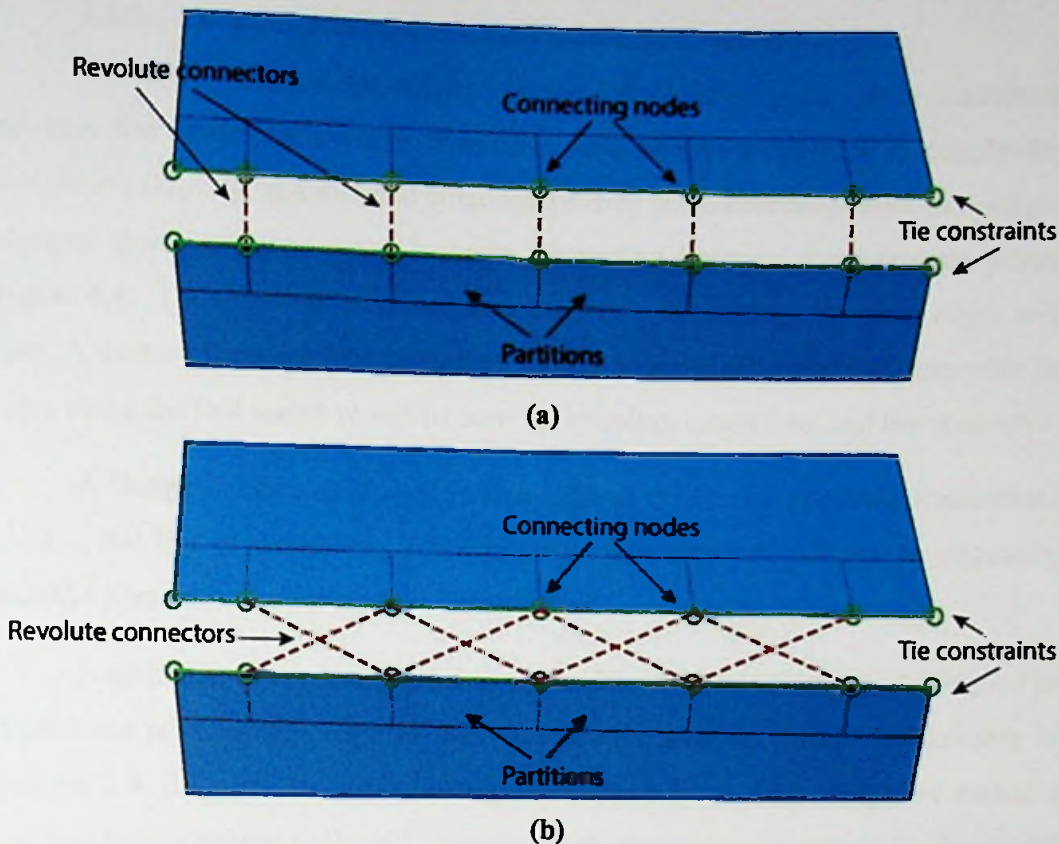
Figure 4.3: Node based connectors (a) perpendicular to fold-line and (b) parallel to fold

removed. Hence for perpendicular connecting method there should be a finite gap in between the shells. The gap in between was set to be the thickness of the membrane.

The moment – angle relationship is incorporated as an elasticity which will be similar to a rotational spring with a spring coefficient (k) where it will follow $M = k \times \theta$. However the experimental relationship was in the form $M = k\,(\theta - \phi)$ with φ being the neutral angle. Equation 3.4, 3.5 and 3.6 were used to find the relationship between fold angle and resistive moment per unit length, which was converted per moment per connector by considering effective length corresponding to each node. The values were input as a non-linear tabular relationship.

Discretising the folded edge into few connecting nodes will impose an error in the analysis. In order to recognise the impact of such errors, a sensitivity analysis was carried out by changing the number of connecting points. The rotational elasticity was uniformly distributed among the connectors and the resulting output was compared.

4.2.2. Coupling Constraint with Rotational Elasticity

Use of a coupling constraint can overcome the need for node – node connectors and ease the modelling process. The basic idea of this method is to couple the translations (U_x, U_y, and U_z) and rotations (R_x) of the connecting edge to a single reference point and then make a single connection between the reference points (Figure 4.4). The fold-line is defined between RP1 - RP2 where the shell edges will meet. A custom local coordinate system should be defined at the fold-line with its x axis along the fold which would be used for coupling constraints and the connector.

A 'hinge' connector is used in this method which can constrain translations (U_x, U_y, and U_z) and rotations (R_x) of the edge. Tie constrain will not be necessary since the connector can ensure the connectivity.

Fold-line stiffness is estimated to full width of the membrane and assigned as a non-linear tabular relationship. It was assumed the moment – angle relationship in equation 3.4, 3.5 and 3.6 can be extrapolated from 0° to 180°. Negative resistive moments before neutral angle will impose an instantaneous acceleration for the model to self-open.

To prevent the rotational spring rotating about the neutral angle in periodic motion, a damping torque is applied. The damping coefficient is decided by trial and error allowing membrane to completely self-open while ensuring the periodic motion dies out within the step time.
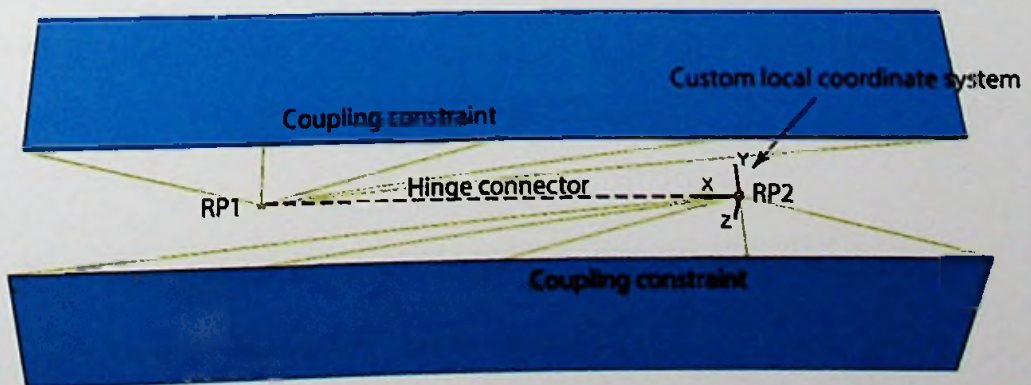
Figure 4.4: Coupling constraint with hinge connector

4.3. Finite Element Solver

Abaqus explicit solver was used for simulations since it can handle complex behaviours such as the dynamic snapping observed in the deployment of a solar sail. However following parameters need to be carefully reviewed when conducting an analysis.

Abaqus/Explicit uses central difference time integration rule where each increment is relatively inexpensive since there is no need for solving a set of simultaneous equations. The explicit central-difference operator satisfies the dynamic equilibrium equations at the beginning of the increment, t. the accelerations calculated at time t are used to advance the velocity solution to time $t + \Delta t$ and the displacement solution to time $t + \Delta t$.

The explicit time integration is conditionally stable, and the stability limit for the operator is given in terms of the highest frequency of the system as

$$\Delta t \leq \frac{2}{\omega_{max}} \left(\sqrt{1 + \varepsilon_{max}^2} - \varepsilon_{max} \right) \qquad\qquad 4.1$$

The time increment Δt is limited by the smallest transit time of a dilation wave across any of the elements in the mesh approximately equal to L_{min}/C_d where L_{min} is smallest element dimension and C_d being dilation wave speed defined in Eq. 4.2. (E and ρ refers to Young's modulus and material density respectively.)

$$C_d = \sqrt{\frac{E}{\rho}} \qquad\qquad 4.2$$

The stability condition of the explicit solver can be verified by investigating the energy balance of the model. In Abaqus/Explicit the energy balance equation is written as

$$E_i + E_{vd} + E_f + E_{ke} - E_w = E_{tot} \qquad\qquad 4.3$$

where,

E_i - internal energy (elastic, inelastic, "artificial" strain energy),

E_{vd} - energy absorbed by viscous dissipation,

E_f - frictional dissipation energy,

E_{ke} - kinetic energy,

E_w - work of external forces

E_{tot} - total energy in the system

If the energy balance is not satisfied and a discrepancy in total energy is observed, the solver has not converged and the analysis will have numerical errors. When using the explicit solver it is important to monitor the energy diagrams to ensure the energy conservation is maintained before extracting the output.

The explicit solver is originally designed for dynamic conditions (high impact) but can also be used for quasi-static analysis. The quasi-static condition can be obtained by limiting the kinetic energy of non-rigid parts to a small fraction (below 5%) of the internal energy.

Computation of a quasi-static analysis at its natural period is impractical due to the need of large increments. Hence the speed of the process is artificially increased to obtain an economical solution. Mass scaling and increased load rates are two approaches of speeding an analysis.

The mass of the elements can be artificially increased which in turn will reduce the dilation wave C_d (Equation 4.2) and increase the minimum time increment Δt. Excessive mass scaling can make the inertia forces more dominant and can increase the kinetic energy of the model.

Some models can experience vibrations leading to high kinetic energy and viscous pressure is an effective way of dampening it quickly and reaching the quasi-static state in minimum increments. The viscous pressure coefficient C_v is typically set to a small percentage (below 2%) of ρC_d.

$$\rho C_d = \rho \sqrt{\frac{E(1-v)}{\rho(1+v)(1-2v)}} \qquad \qquad 4.4$$

Viscous pressure coefficient of 1×10^{-7} was applied to the model.

4.4. Results

4.4.1. Element Sensitivity Analysis

Energy checks and computational time was compared to identify the most suitable element type. Figure 4.5 illustrates the artificial energy during the analysis for each element type. S4RS elements exhibited the highest artificial energy while other quadrilateral elements with reduced integration (S4R and S4R(h)) also indicated high numerical instabilities. However S4 element and triangular elements were free from artificial energy build-up.

Table 4.1 compares the computational cost of the shell elements. Same processing power was used for all instances and the CPU time was normalized by taking S3R as 100%. Accordingly S4 elements proved to be computationally costly while reduced integration drastically reduced the simulation time. Considering the artificial energy diagrams, triangular elements were proved to be more suitable for the analysis.
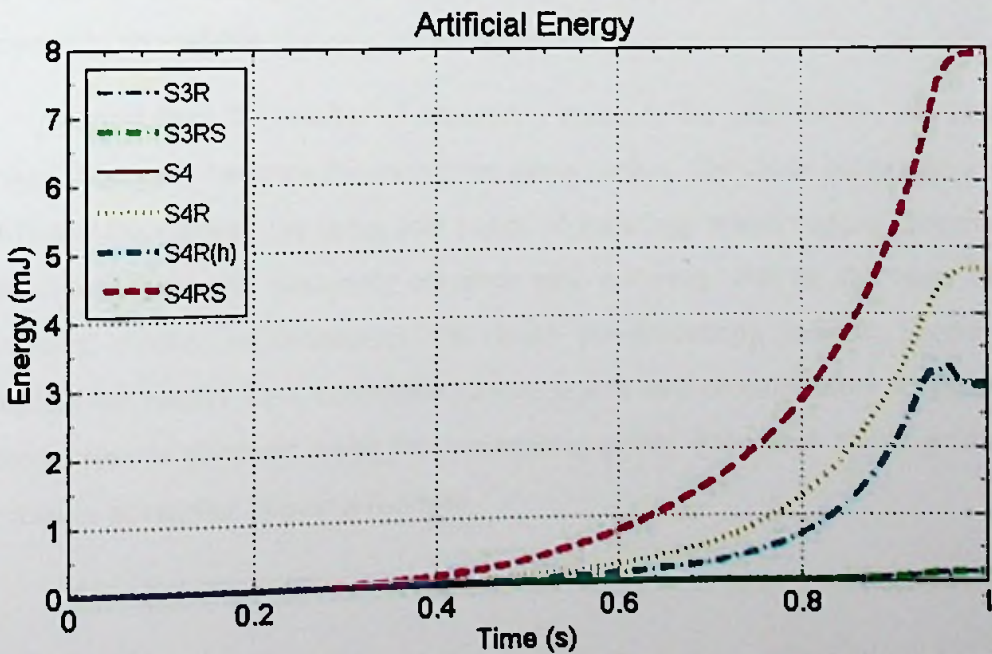
Figure 4.5: Artificial energy diagram for conventional shell elements

34

Table 4.1: Computational time (normalized) for conventional shell elements

Element	Normalized computational time
S4	200%
S4R	46%
S4R(h)	34%
S4RSW	71%
S3R	100%
S3RS	54%

4.4.2. Node based vs. coupling constrained approach

Two configurations were introduced for node – node connectors which aligns them perpendicular and parallel to the fold-line. Both methods produced similar results for the symmetric case considered. But in an asymmetric model connectors defined parallel could become erroneous since top and bottom portions are connected at different points along the fold. It was further noted, parallel method requires higher number of connectors to be defined between given number of connecting points.

Theoretically two folded portions cannot overlap the same space and they will be at a distance equal to membrane thickness which could be used to define the connectors perpendicularly. Hence it was concluded perpendicular arrangement to be preferred in an analysis.

Impact from the number of connecting points to the analysis was assessed by varying them and observing the membrane stress profile. The actual hinge response is distributed through-out the entire fold (since no scouring) which suggests increasing connecting points will positively correlate with accuracy. But on the other hand, increasing number of connectors will make pre-processing tedious. Figure 4.6 compares the results for 3 connectors, 5 connectors and 10 connectors. High stress concentration is observed when few connecting points were used and it gradually diminishes as number of points increase.
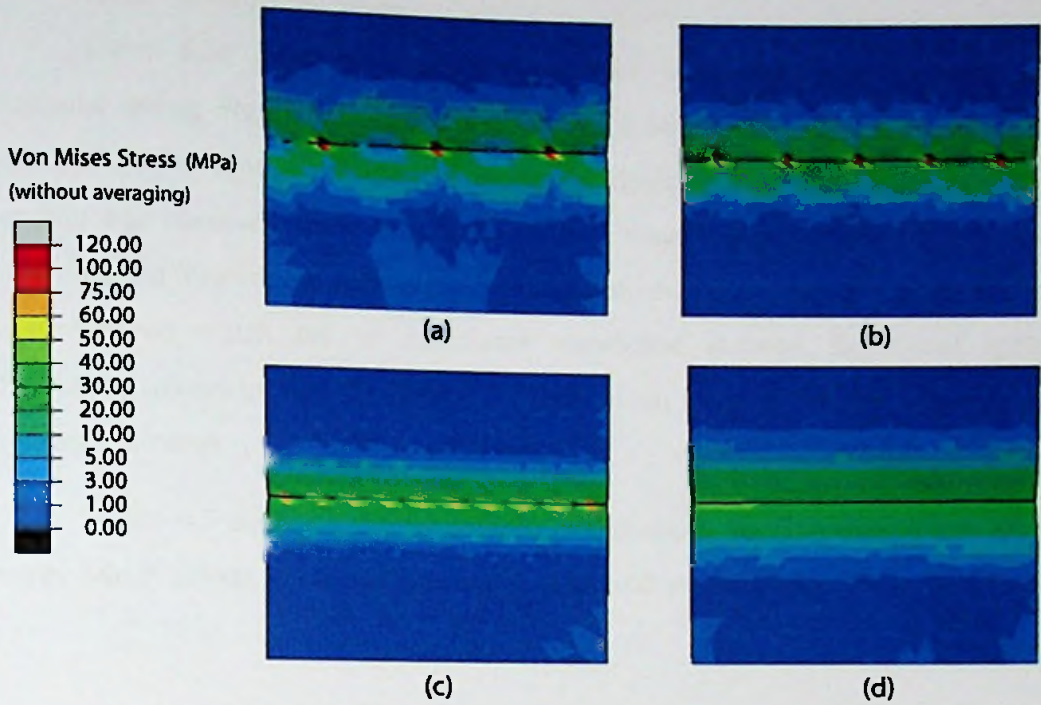
Figure 4.6: Membrane stress profile with (a) 3 connecting points, (b) 5 connecting points, (c) 10 connecting points and (d) coupling constraint

Figure 4.6 (d) is the coupling constrained approach where no stress concentration can be observed. It can be used with following assumptions.

(i)   The opening angle is constant through-out the fold

– Since the rotation of edges are coupled to a single reference points they are maintained same within the fold.

(ii)   The fold remains straight during unfolding

– The translations of the edges are constrained by the local coordinate system defined along the fold. The edge can only rotate globally with its coordinate system

Since whole edge is connected to a single node, stress variation along the membrane cannot be observed. Hence this approach is preferred for a symmetric model or for a model with less accuracy.

4.4.3. Fold Idealization

Three fold idealization approaches were compared; pinned, fixed and rotational spring. Figure 4.7 illustrates deformation and membrane stress profiles for each method. Membrane unfolding under pinned idealization remained straight and no bending was observed while membrane stresses remained negligible. On the other hand, in fixed idealization fold angle did not open and high curvatures in membrane was observed which led to significant membrane stresses. Rotational spring idealization allows to vary the spring stiffness which controls the fold opening and membrane stresses.

Figure 4.7 confirms the importance of balancing bending energy and hinge energy which affects the deformation profile as well as membrane stress profile. To
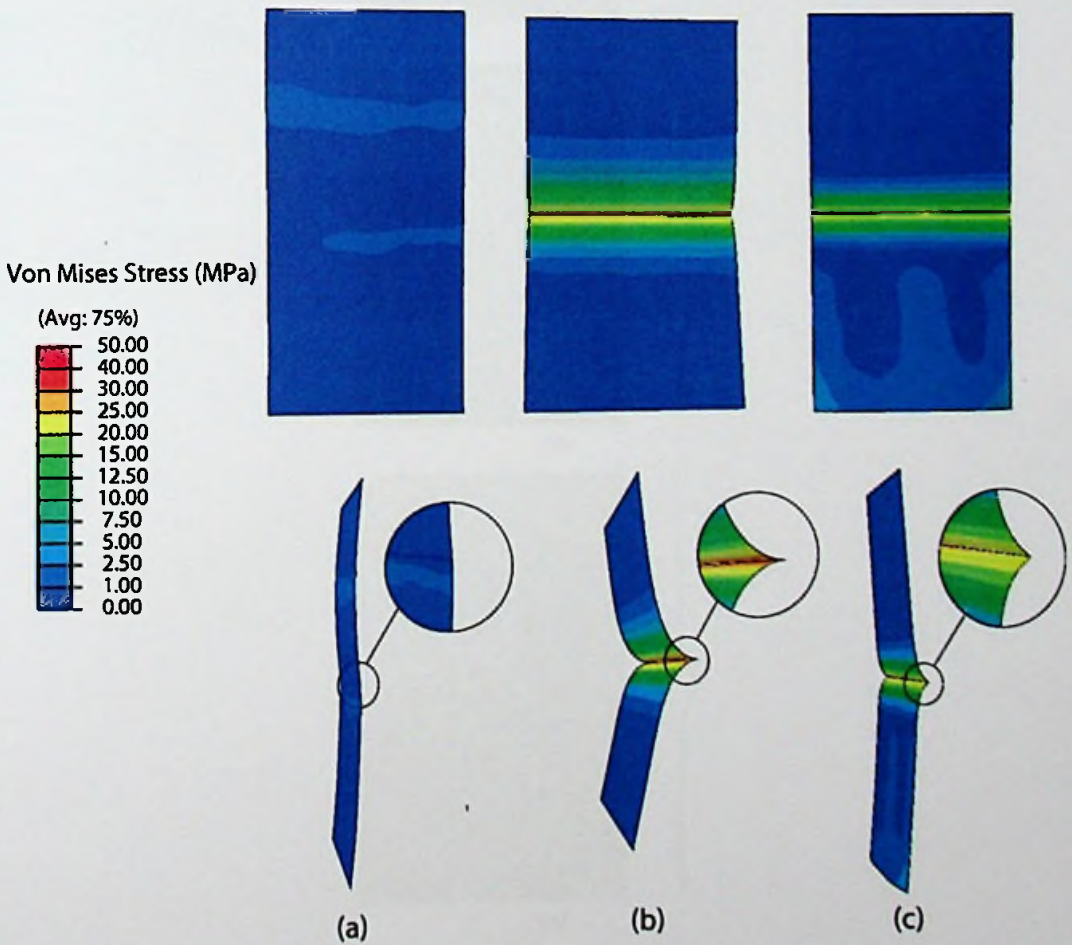
Figure 4.7: Stress distribution and deformation profile comparison of (a) pinned, (b) fixed and (c) rotational spring idealizations

verify the deformation profile, boundary condition was modified from displacement to a point load.

Figure 4.8 compares experimental and finite element model deformations for 200 HN Kapton membrane under different loading conditions. It can be observed that rotational spring idealization has captured the actual deformation profile of the membrane.
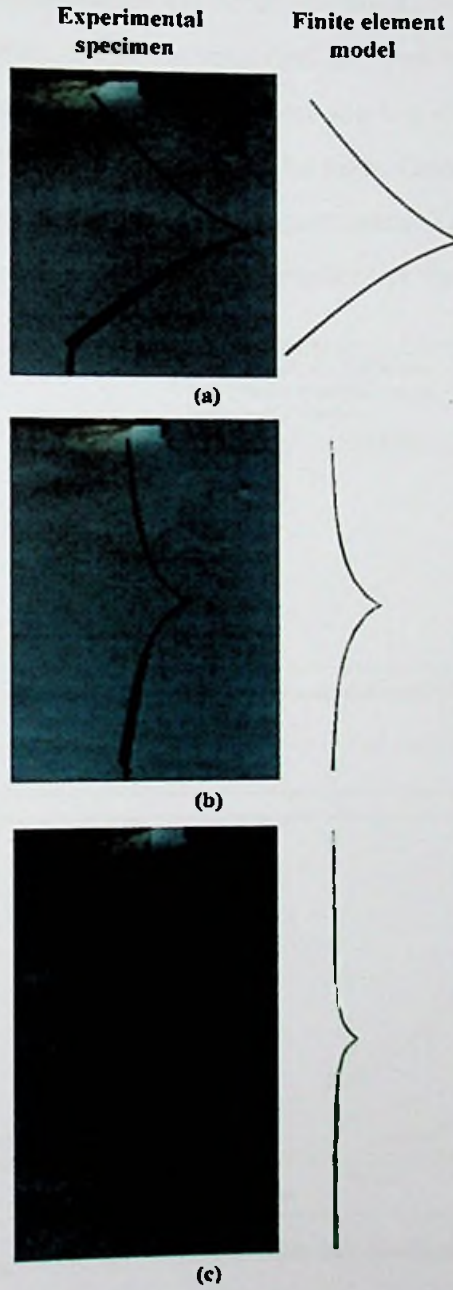
Figure 4.8: Comparison of experimental and simulation deformation profiles for Kapton 200HN at (a) 0.002 N , (b) 0.027 N and (c) 0.159 N

Since significant variations in the deformation profile was observed depending on loading, fold-line stiffness and neutral angle unfolding forces were plotted against the displacement of the bottom edge.

Figure 4.9 compares the force required to unfold the membrane during 4 idealization approaches; Perfect hinge, Perfect weld and rotational springs with two neutral angles. Perfect hinge idealization requires zero force to unfold where the fold is free to open and no membrane bending is observed. Weld idealization is having the largest forces where membrane opening is restricted and high bending is observed in membrane. Rotational spring idealization is between the two extremes and when the neutral angle is lower, unfolding forces tend to be high. Overall, final 25% of the displacement is producing the significant force requirements. This confirms that for a given force magnitude, maximum deflection is dependent on the fold-line stiffness.
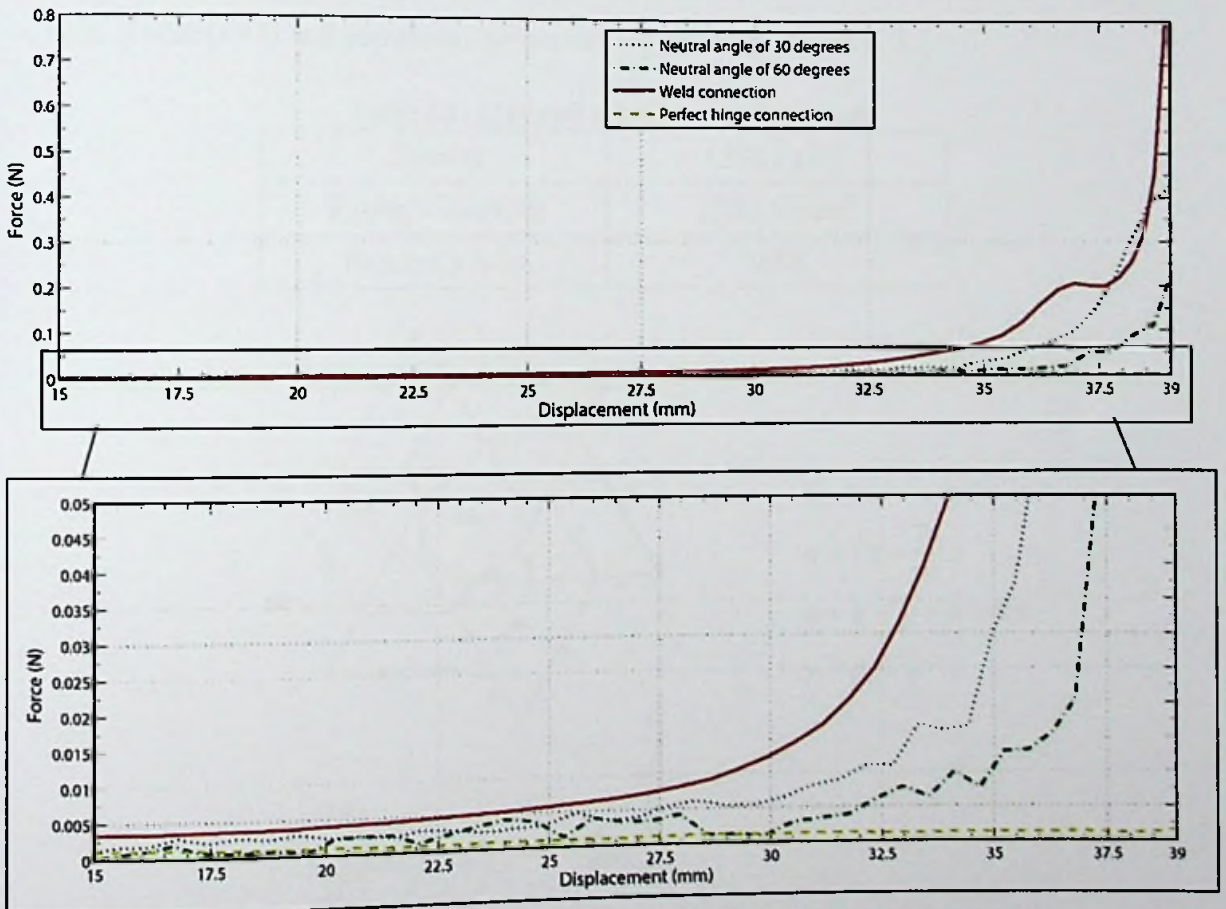
Figure 4.9: Unfolding forces for different fold-line idealization approaches

CHAPTER V

5. APPLICATION OF FOLD-LINE STIFFNESS FOR THE DEPLOYMENT OF A SOLAR SAIL

Following section investigates the importance of incorporating fold-line stiffness during the deployment phase of a solar sail. An experimental study carried out at space structures laboratory of California Institute of Technology has been used for this purpose (Arya & Pellegrino, 2014).

5.1. Experimental Setup Details

A brief description about the experimental setup is as follows. Solar sail geometry has been developed based on the wrapping patterns suggested by Guest (1994) as illustrated in Figure 5.1 Octagonal polygonal hub ($n = 8$) was used with eight radial tabs ($j = 8$) and membrane properties are indicated in Table 5.1.

Table 5.1: Material properties of Solar sail

Density	1390 kg/m^3
Young's modulus	5200 N/mm^2
Poisson's ratio	0.38

$$\alpha = \left(1 - \frac{2}{n}\right)\pi$$

$$\alpha + \beta + \gamma + \delta = 2\pi$$

$$\gamma - \beta = \frac{\pi}{2}$$
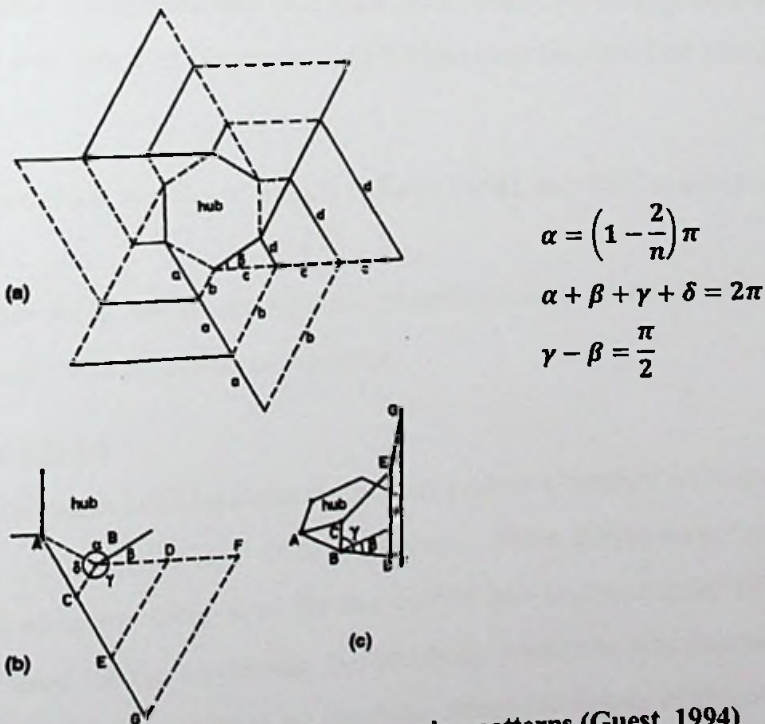
Figure 5.1: Formulation of wrapping patterns (Guest, 1994)
(a) hexagonal polygon, (b) detailed view of angles and (c) folded configuration
(n is the number of sides of the polygon)
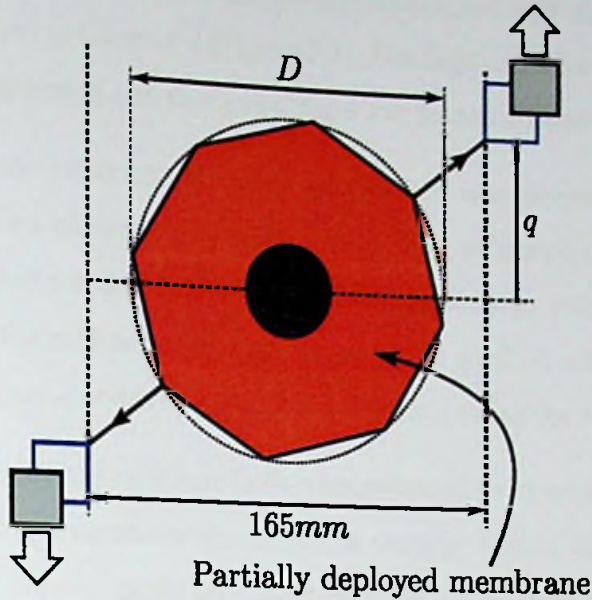
Figure 5.2: Experimental setup (Arya & Pellegrino, 2014)

Weight off-loads were used to minimize gravitational effects and to support the structure at the centre of hub allowing the solar sail to rotate around its centroid axis. Effect of air drag is reduced by controlling the rate of deployment (at 0.78 mm/s) and unfolding it quasi-statically. Figure 5.2 is a schematic of deployment during the experiment. Two force sensors have been used to record the deployment forces.

Membrane was pre-creased with laser perforations where approximately 36% of the material was removed. Two types of fold-lines can be identified based on their fold angle;

(i)   Major folds, which are aligned radially folded upto 180° at compacted state and

(ii)   Minor folds, which are aligned circumferentially where the membrane is folded by 22.5° during compaction.

5.2. Numerical Model

A finite element model was developed using Abaqus/Explicit software package consisting of 13006 nodes and 19941 elements. Three dimensional hexahedral (C3D8R) solid elements were used for the central hub and triangular (S3R) shell elements were used for the membrane. A rigid body constraint was imposed on the solid hub since our present focus is on the deployment mechanics of the membrane.

The membrane was modelled with eight portions connected with different idealization approaches discussed in Chapter 4 (Figure 5.3). Connections were initially defined at the deployed configuration and then membrane was folded around the hub.

Similar to the experimental setup, central hub was supported at its centroid using a pin constraint allowing it to rotate freely. Two reference nodes were defined 165 mm apart (as indicated in Figure 5.2) and *link* connectors were defined from the reference node to the mid-point of outer edges of the shell. A smooth displacement was applied at reference nodes in opposite directions opening the sail.

Rotational stiffness of minor folds were assumed to be negligible compared to major folds. Empirical equations developed in chapter 3 were used to estimate the fold-line stiffness. Neutral angle was assumed to be 30 degrees since actual values were not measured. In order to highlight the variation of fold-line stiffness, 4 cases were considered in the analysis as indicated in Table 5.2. Node based connectors were defined with each approximately representing 4 mm length along the fold-line. The overall rotational stiffness of a fold-line was adjusted to account for 36% scouring.
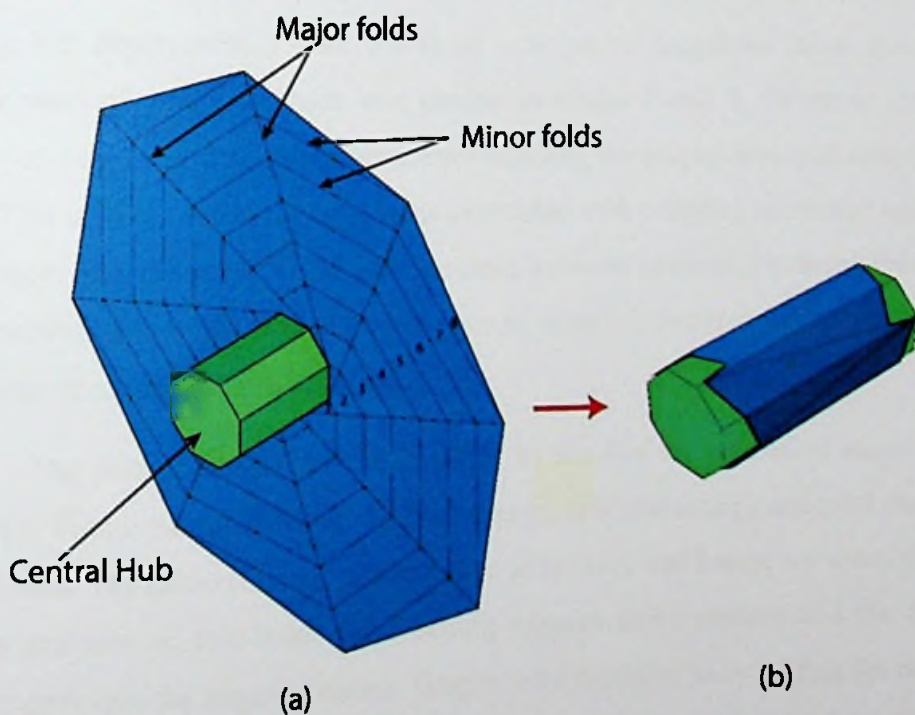
Figure 5.3: Finite element geometry of the solar sail (a) before folding and (b) after folding

	Hinge idealization	Connection	Membrane
Model 1	Perfect hinge	Tie	100HN
Model 2	With rotational spring	Tie, node – node connectors	100HN
Model 3	With rotational spring	Tie, node – node connectors	300HN
Model 4	With rotational spring	Coupling constraints	100HN

Viscous pressure coefficient (C_v) of 1×10^{-7} was applied to dampen out the vibrations in the model and control the kinematic energy. Displacement load was applied over 5 seconds with smooth step amplitude definition reduce initial accelerations in the model. Mass scaling was setup with minimum integration step as 1×10^{-6} seconds to speed up the simulation.

5.3. Simulation Results

Displacement field outputs were recorded to observe the deformation path during the deployment. Figure 5.4 is of a series of snapshots taken during the deployment of model 2 which was similar to model 1 and 3. However model 4, deployed peculiarly with its membrane not attaining the proper deployed state (Figure 5.5). This is likely due to the conditions associated with coupling constraint where the fold has to remain straight and the fold opening has to be uniform, hindering the natural deformation path of the sail. Hence the use of coupling constraint is not suitable for complex structures such as solar sails.

The energy diagrams were recorded to identify the numerical errors in the analysis. Figure 5.6 tabulates the internal energy, artificial energy and total energy of the models. The initial (folded) configuration of model 2 and 3 were not stress free due to the presence of fold-lines. Self-opening releases these stresses and the internal energy goes into the negative region. Graphs were modified to by adding the negative internal energy and keeping it in the positive region. In all three model total energy is zero which suggest that the solution has been converged. However artificial energies
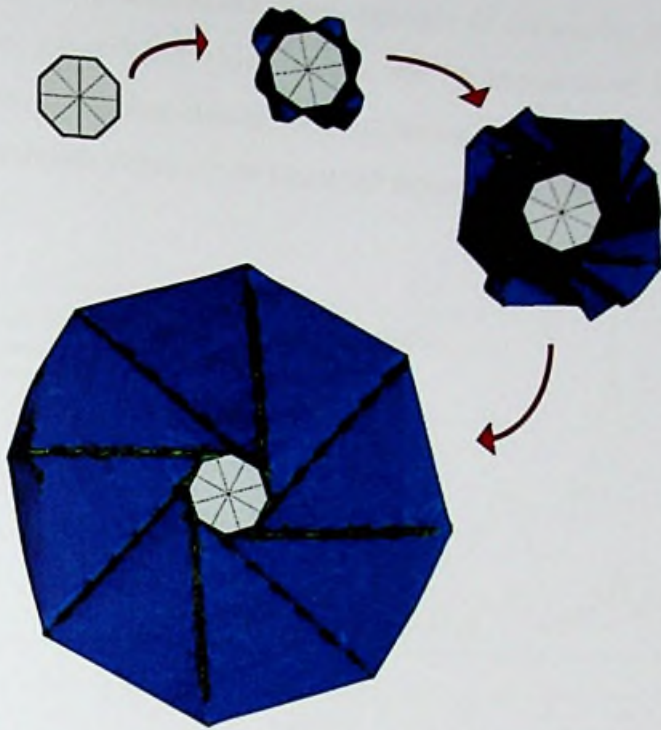
Figure 5.4: Sequence of snapshots taken during the deployment of model 3

have totalled around 5% - 10% of internal energy which suggests further investigations can improve the model. These could be due to vibrations in the membrane, due to general contact or stress singularities in the membrane.

(a)

(b)
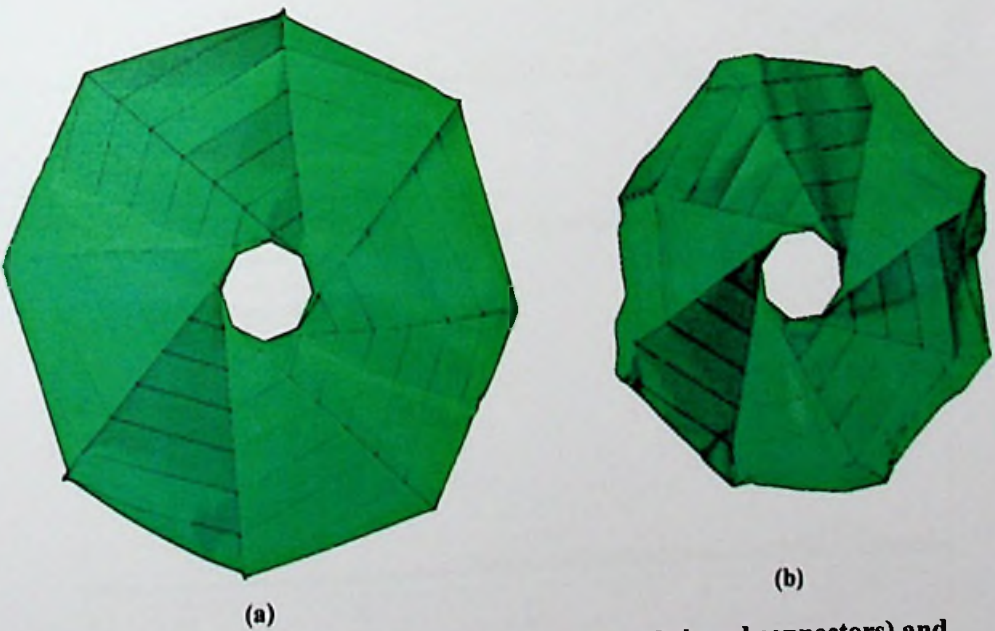
Figure 5.5: Deployed state of (a) model 2 (node based connectors) and (b) model 4 (coupling constrained connectors)

The experiment was carried out quasi-statically to reduce the air resistance during the physical experiment which would not be encountered in a virtual environment. Dynamic snapping effects observed during deployment induce sudden vibrations in the membrane which can be identified through the spikes in the kinematic energy of the model.
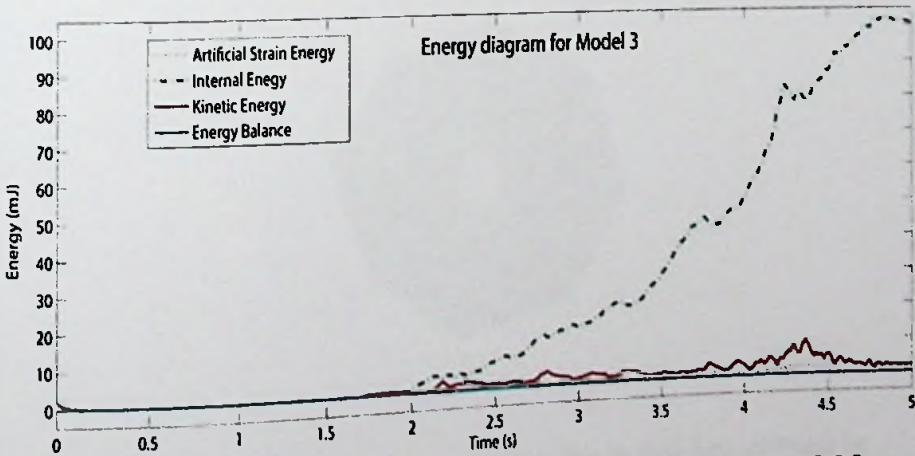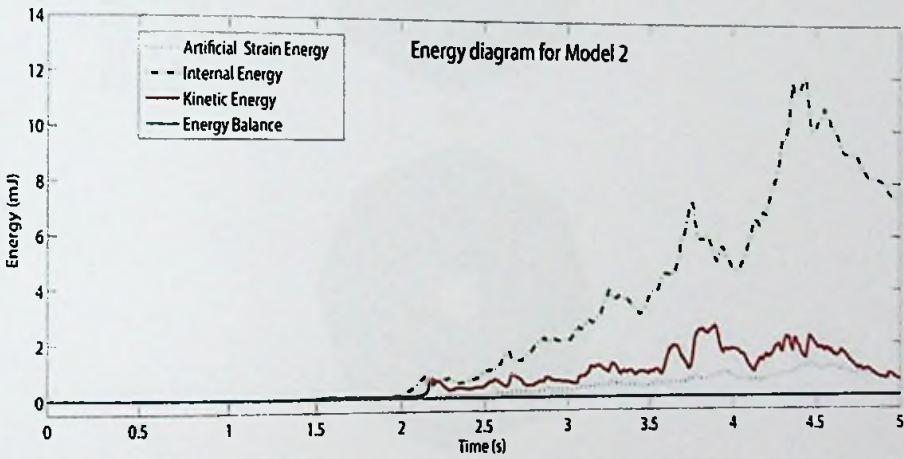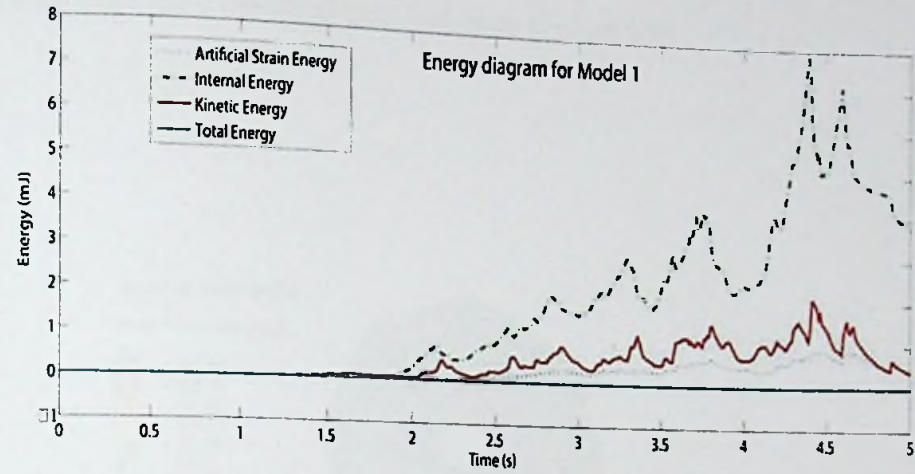
Figure 5.6: Energy plots recorded for model 1, model 2 and model 3

Figure 5.7 examines the deployed stress profile of the membrane for each instance where significant variations can be observed depending on the idealization approach (model 1 and model 2). Furthermore, an increase in the membrane thickness prominently escalate the stress values as shown in model 3. Papa & Pellegrino (2008) have investigated the membrane stresses for a flat sheet with Miura pattern where similar stresses were observed near fold-lines (Figure 5.8).
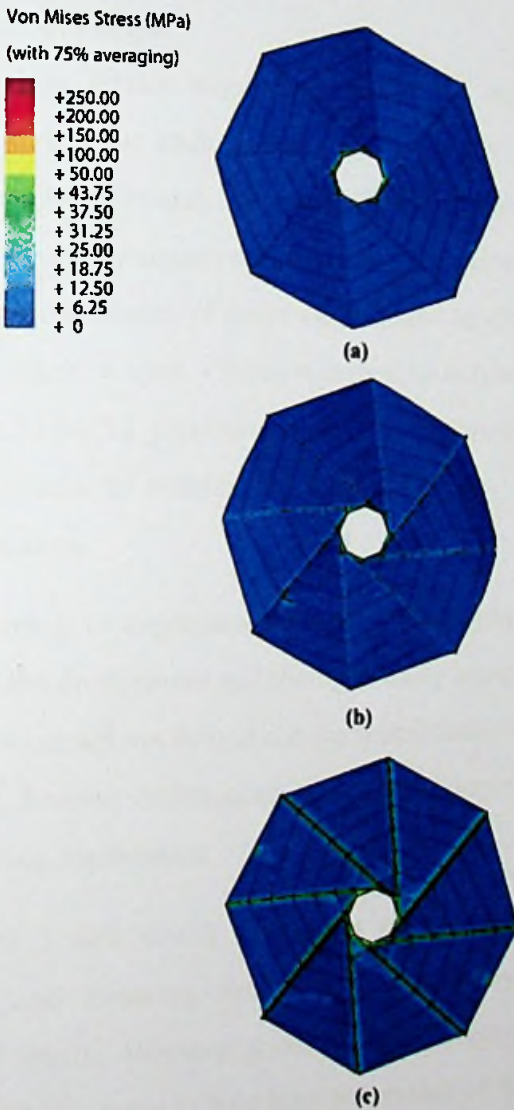
Figure 5.7: Membrane stress generation due to fold-line stiffness in (a) model 1, (b) model 2 and (c) model 3
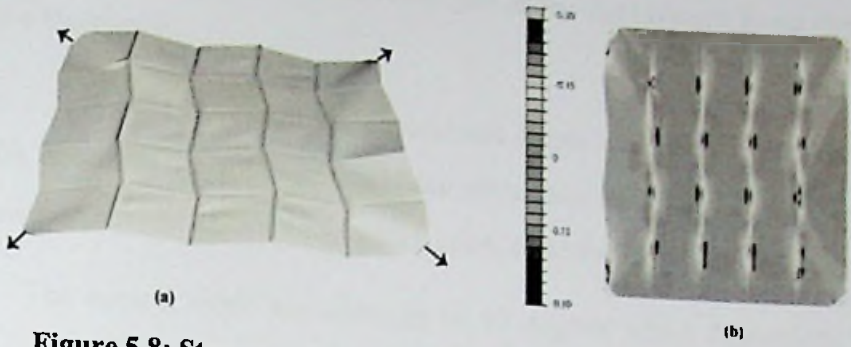
Figure 5.8: Stress profile around fold-lines for Miura pattern (a) applied force and (b) midplane normal stress components in MPa (Papa & Pellegrino, 2008)

5.4. Deployment Forces

Reaction forces were recorded at the reference node to compare the deployment forces for each idealization approach. The experimental forces were plotted against the percentage deployed (D/D_f) where D is the current diameter of the model and D_f is the maximum possible diameter. For comparisons, a similar graph was plotted using coordinates of outer edge nodes to determine the current. MATLAB function *smooth (x, y, span, rloess)* was used to reduce the noise of raw data where the span was set to be 0.1 (Mathworks, 2017). Experimental data was shifted down by 0.14 in D/D_f axis to overlap the starting points. Figure 5.9 compares the final deployment forces.

According to experimental results, the deployment forces are around 0.1 N until 65% of the deployment and then gradually increase up to 1 N. The experimental setup was not carried out fully since the membrane collapsed when the fold-line were fully opened. Several intermediate peaks are observed which correspond to dynamic snapping during deployment.

Model 1 and model 2 requires similar forces during initial 50% of the deployment and contains similar spikes initially which correspond with the experimental results. However model 1 fails to recognize the force increment in the final stages. There seems to be a high estimation of the forces between 0.4 and 0.6 of deployment. This could be due to the difference in deployment rate between simulation

and experiment. Model 3 predicts about 400% rise in the deployment force due to thickness of the membrane.

Model 2 was able to predict the deployment forces accurately compared to model 1 which confirms the applicability of the simulation technique. However the analysis is based on several assumptions which needs to be further clarified.

(i) The neutral angle was assumed be 30 degrees which determines the moment – angle relationship. This could have slight modifications to the force plot.

(ii) The scouring effect can be captured by reducing effective length of fold.

(iii) Interaction between folds is negligible.
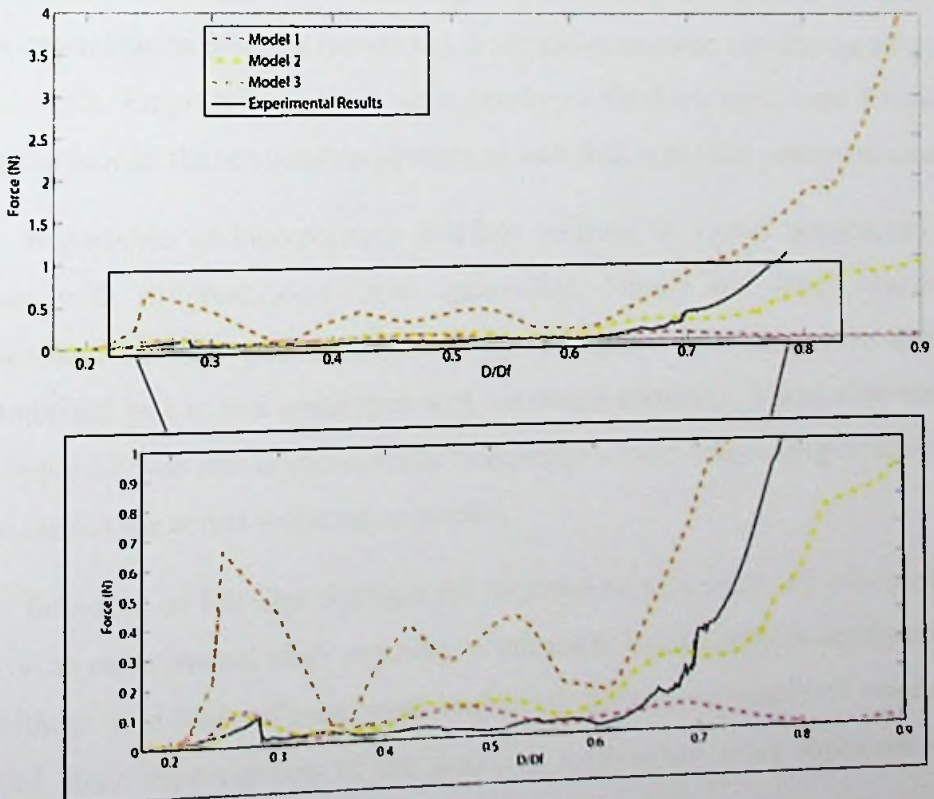
Figure 5.9: Deployment forces for the solar sail

CHAPTER VI

6. CONCLUSIONS AND FUTURE WORKS

6.1. Conclusions

Behaviour of foldable membrane structures are purely depended on the arrangement of fold-lines, allowing them to display unique properties. Fold-line mechanics of thin membranes were investigated in this thesis and it was identified that hinge response could be best idealised as a rotational spring. When a fold-line is formed, plastic deformations can be observed in the membrane. Kinked shape of the fold and membrane stresses exerts a self-opening torque at fully folded state and attains to the stress free neutral angle.

Opening or closing of the neutral angle generates a resistive moment at the fold which can be quantified using moment – angle response. When the membrane is unfolded, its deformation profile is a resultant of membrane bending and fold opening. An experiment was designed to measure moment – angle response for Kapton HN polyimide. Variation of fold-line stiffness with membrane thickness was recorded for 25 μm, 50 μm and 75 μm thick membranes. It was further noted, neutral angle of the fold is dependent on creasing factors and the resistive moment can change along with neutral angle. Empirical equations were developed for three membrane thicknesses which can predict the relationship between current fold angle and generated moment.

Importance of incorporating fold-line stiffness in virtual simulations were assessed with different idealization approaches. Pinned and fixed connections represented minimum and maximum hinge energies while the novel approach recommended was to use connectors with rotational elasticity. It was observed that novel approach was able to successfully incorporate correct hinge energies which was able to predict the actual deformation profile.

Influence of fold-line stiffness for deployment of a solar sail was evaluated based on an experimental study available in literature. Virtual deployment forces with and without fold-line stiffness were compared against experimental results and observed clear improvements of the predicted loads when using rotational spring

idealization. Model with fold-line stiffness was able to capture membrane stresses around folds. It should be further noted that the experimental study is a scaled model with lesser number of folds which can supress the significance of hinge response.

6.2. Recommendations for Future Work

Predicting the behaviour of foldable membrane structures is still at a primitive stage and requires further analysis. Even though incorporation of hinge response has yielded true deformation profile, membrane stresses have not been validated. Use of digital image processing tools can generate membrane stress profiles which can be used for validations.

One of the critical assumptions on this thesis is the uniform behaviour of a fold, where it opens symmetrically. Hinge response of an asymmetric fold can be a different scenario and needs to be investigated. Complex folding patterns (i.e. Miura-Ori) have vertices resulting from many fold-lines, where interaction between folds can get significant.

It was observed that behaviour of fold-lines are due to localised plastic deformations resulting in a kinked shape. Although extensive literature is available on paperboard, deformation of more durable materials (such as Kapton and Mylar) are limited. It is recommended to carry microscopic investigations on the plastic behaviour of material.

REFERENCES

Abaqus Documentation. (2014). *Anaylsis User's Guide (ver 6.13).* Providence, Rhode Island: Dassault Systemes Simulia Corp. Retrieved 2017

Abbott, A. (2014). *Characterization of Creases in Polymers for Adaptive Origami Engineering.* The School of Engineering. Dayton, Ohio: University of Dayton.

Arya, M., & Pellegrino, S. (2014). Deployment mechanics of highly compacted thin membrane structures. *Spacecraft Structures Conference.* National Harbor, Maryland: AIAA SciTech Forum.

Baldwin, A. (2015). *origami jumping frogs: easy folding instructions.* Retrieved June 20, 2017, from Its always autumn: http://www.itsalwaysautumn.com/2015/03/06/origami-jumping-frogs-easy-folding-instructions.html

Beex, L., & Peerlings, R. (2009, December). An experimental and computational study of laminated paperboard creasing. *International Journal of Solids and Structures, 46*(24), 4197-4207.

Dharmadasa, B. (2016). *Simulation of crease stiffness in thin membranes.* Department of Civil Engineering. Moratuwa: University of Moratuwa.

Dupont. (2017). *DUPONT Kapton; Summery of properties.* Technical Data sheet.

Goddard Space Flight Center, N. (2017, May 05). Retrieved from https://www.nasa.gov/feature/goddard/2017/nasa-s-new-shape-shifting-radiator-inspired-by-origami

Guest, S. (1994). *Deployable structures: Concepts and analysis.* Cambridge: University of Cambridge.

Lechenault, F., Thiria, B., & Adda-Bedia, M. (2014, June 20th). The mechanical response of a creased sheet. *Physical Review Letters, 112*(24), 244301.

Liyanage, P., & Mallikarachchi, H. (2013). Origami based folding patterns for compact deployable structures. *4th International Conference for Structural Engineering and Construction Management.* Kandy, Sri Lanka: 4th

International Conference for Structural Engineering and Construction Management.

Mathworks. (2017). *MathWork curve fitting*. Retrieved June 20, 2017, from MathWorks.com:

https://in.mathworks.com/help/curvefit/smooth.html?searchHighlight=smooth%20rloess&s_tid=doc_srchtitle

Miura, K. (1989). Map fold a La Miura style, Its physical characteristics and application to the space science. *First international meeting of origami science and technology*. Italy: KTK scientific publisher.

NASA. (2005). *Solar sail propulsion*. Retrieved June 20th, 2017, from https://www.nasa.gov/pdf/134645main_solar_sail_fs.pdf

Natori, M., Sakamoto, H., Katsumata, N., Yamakawa, H., & Kishimoto, N. (2014). Conceptual model study using origami for membrane space structures – a perspective of origami-based engineering. *Mechanical Engineering Reviews, Vol. 2 (2015)*(No. 1), 14-00368-14-00368.

Okuizumi, N., & Yamamoto, T. (2009, January). Centrifugal deployment of membrane with spiral folding: Experiment and Simulation. *Journal of space engineering, 2*(1), 41-50.

Overvelde, J., Weaver, J., Hoberman, C., & Bertoldi, K. (2017). Rational design of reconfigurable prismatic architected materials. *Nature, 541*, 347-552.

Papa, A., & Pellegrino, S. (2008). Systematically Creased Thin-Film Membrane Structures. *Journal of Spacecrafts and Rockets*, 10-18.

Sakamoto, H., Natori, M., Kadonishi, S., Satoua, Y., Shirasawac, Y., Okuizumic, N., . . . Okumaa, M. (2014). Folding patterns of planar gossamer space structures consisting of membranes and booms. *Acta Astronautica, 94*(1), 34-41.

Schenk, M. (2011). *Folded Shell Structures*. Cambridge: PhD thesis at University of Cambridge.

Shirasawa, Y., Mori , O., Miyazaki, Y., Sakamoto, H., Hasome, M., Okuizumi, N., . .
. Kawaguchi, J. (2011). Analysis of Membrane Dynamics using Multi-Particle
Model Solar Sail Demonstrator "IKAROS". *52nd
AIAA/ASME/ASCE/AHS/ASC Structures, Structural Dynamics and Materials
Conference.* Denver, Colorado: 52nd AIAA/ASME/ASCE/AHS/ASC
Structures, Structural Dynamics and Materials Conference, Structures,
Structural Dynamics, and Materials Conference.

Sickinger, C., & Breitbach, E. (2004). Ultra-light weight deployable space structures.
Loughborough,England: 4th International conference on thin-walled
structures.

Sleight, D., Michii, Y., Lichodziejewski, D., Derbes, B., Mann, T., Slade, K., & Wang,
J. (2005). Finite element analysis and test correlation of a 10-meter inflation
deployed solar sail. *46th AIAA/ASME/ASCE/AHS/ASC Structures.* Austin,
United States: 46th AIAA/ASME/ASCE/AHS/ASC Structures, Structural
Dynamics and Materials Conference.

Wang, C., Du, Z., Tan, H., & Xie, J. (2011). Shearing-wrinkling behaviour of creased
rectangular membrane. *Acta Mechanica Sinica, 27*, 550-558.

Wang, C., Tan, H., & He, X. (2010). Wrinkle-crease interaction simulation using
combined MT model and DP technique. *51st AIAA/ASME/ASCE/AHS/ASC
Structures, Structural Dynamics, and Materials Conference.* Orlando, Florida:
51st AIAA/ASME/ASCE/AHS/ASC Structures, Structural Dynamics, and
Materials Conference.

Yasuda , H., Yein, T., Tachi, T., Miura, K., & Taya, M. (2013). Folding behaviour of
techi-miura polyhedron bellows. *Proceedings of The Royal Society A
Mathematical Physical and Engineering Sciences, 469*(2159), 20130351.

APPENDIX I: MOMENT – ANGLE DATA

Membrane	Test Specimen	Load (N)	x (mm)	Angle(degrees)	Moment per unit length (Nmm/mm)
100HN	1	0.000		37	0.0000
		0.001	8.12	41	0.0008
		0.003	5.89	42	0.0017
		0.005	4.96	43	0.0024
		0.010	3.69	48	0.0036
		0.015	3.14	51	0.0046
		0.020	2.63	58	0.0052
		0.032	2.02	63	0.0065
		0.044	1.63	70	0.0072
		0.069	1.26	74	0.0087
		0.094	0.99	78	0.0093
	2	0.000		50	0.0000
		0.001	7.86	54	0.0008
		0.003	5.94	57	0.0017
		0.005	4.92	62	0.0024
		0.010	3.77	65	0.0037
		0.015	3.17	63	0.0047
		0.020	2.68	68	0.0053
		0.032	2.14	74	0.0068
		0.044	1.72	74	0.0076
		0.069	1.37	83	0.0095
		0.094	1.15	90	0.0108
	3	0.000		73	0.0000
		0.001	5.98	73	0.0006
		0.003	4.37	75	0.0013
		0.005	3.61	76	0.0018
		0.010	2.67	81	0.0026
		0.015	2.32	82	0.0034
		0.020	1.95	86	0.0038
		0.032	1.59	90	0.0051
		0.044	1.35	91	0.0060

Membrane	Test Specimen	Load (N)	x (mm)	Angle(degrees)	Moment per unit length (Nmm/mm)
100HN	4	0.000		77	0
		0.001	7.08	82	0.0006
		0.002	5.7	84	0.0011
		0.004	4.47	84	0.0017
		0.007	3.57	86	0.0024
		0.010	3.03	91	0.0029
		0.015	2.65	91	0.0038
		0.020	2.23	93	0.0043
		0.032	1.87	98	0.0059
		0.044	1.66	98	0.0073
		0.069	1.35	102	0.0093
	5	0.000		91	0
		0.001	4.58	92	0.0004
		0.003	3.28	94	0.0009
		0.005	2.87	94	0.0014
		0.010	2.16	95	0.0021
		0.015	1.85	97	0.0027
		0.020	1.51	103	0.0029
		0.032	1.25	105	0.0039
		0.044	1.1	107	0.0048
		0.069	0.87	111	0.006
	6	0.000		110	0
		0.001	3.5	112	0.0003
		0.003	2.56	114	0.0007
		0.005	2.21	115	0.001
		0.010	1.73	117	0.0016
		0.015	1.47	121	0.0021
		0.020	1.34	123	0.0026
		0.032	0.93	122	0.0029
		0.044	0.72	122	0.0031
		0.069	0.62	124	0.0042

Membrane	Test Specimen	Load (N)	x (mm)	Angle(degrees)	Moment per unit length (Nmm/mm)
200HN	1	0.000		36	0
		0.002	19.5	40	0.0038
		0.005	15.57	44	0.0076
		0.010	12.16	47	0.0119
		0.015	9.89	50	0.0146
		0.027	7.78	53	0.0211
		0.039	6.29	56	0.0248
		0.064	4.83	60	0.031
		0.089	4.06	62	0.0361
		0.151	2.95	69	0.0445
		0.295	1.9	83	0.056
	2	0.000		45	0
		0.002	17.51	50	0.0034
		0.010	11.25	52	0.011
		0.027	7.26	56	0.0197
		0.039	6.01	63	0.0237
		0.052	5.13	63	0.0266
		0.077	4.16	69	0.0318
		0.118	3.23	79	0.038
		0.159	2.71	82	0.0431
	3	0.000		74	0
		0.001	17.3	77	0.0017
		0.005	12.89	81	0.0063
		0.010	10.1	85	0.0099
		0.022	6.87	87	0.0152
		0.035	5.56	91	0.0192
		0.059	4.21	95	0.0249
		0.084	3.25	98	0.0273
		0.125	2.61	104	0.0327
	4	0.000		88	0
		0.002	13.69	92	0.0027
		0.015	7.16	98	0.0105
		0.027	5.2	100	0.0141
		0.064	3.17	103	0.0203
		0.089	2.7	104	0.024
		0.151	2.24	110	0.0338

Membrane	Test Specimen	Load (N)	x (mm)	Angle(degrees)	Moment per unit length (Nmm/mm)
300HN	1	0.000		42	0.0000
		0.005	18.75	47	0.0092
		0.010	16.53	49.6	0.0162
		0.022	13.13	49	0.0291
		0.047	10.27	53.1	0.0482
		0.072	8.45	52.65	0.0605
		0.096	7.26	57.8	0.0699
		0.138	6.1	58	0.0839
		0.179	5.37	58.6	0.0960
	2	0.000		43	0.0000
		0.005	16.85	46	0.0090
		0.010	15.9	47	0.0163
		0.022	13.6	50	0.0302
		0.047	10	53	0.0469
		0.072	8.2	56	0.0587
		0.096	7.04	56	0.0678
		0.138	5.84	58	0.0803
		0.179	5.13	59	0.0917
		0.220	4.55	61	0.1001
		0.282	3.92	66	0.1104
		0.426	3.19	68	0.1359
	3	0.000		76	0.0000
		0.002	15.6	76	0.0032
		0.005	14.01	78	0.0071
		0.010	12.71	78	0.0125
		0.022	10.11	79	0.0224
		0.035	8.4	81	0.0290
		0.059	6.58	80	0.0390
		0.084	5.66	82	0.0475
		0.105	4.99	86	0.0522
		0.125	4.54	88	0.0568

Membrane	Test Specimen	Load (N)	x (mm)	Angle(degrees)	Moment per unit length (Nmm/mm)
300HN	4	0.000		86	0.0000
		0.005	12.54	86	0.0066
		0.010	11.27	88	0.0115
		0.022	9.41	90	0.0209
		0.047	6.8	91	0.0319
		0.072	5.47	95	0.0392
		0.096	4.7	98	0.0453
		0.138	3.92	98	0.0539
		0.179	3.04	101	0.0543
		0.220	2.98	100	0.0655
		0.282	2.6	100	0.0733
	5	0.000		107	0.0000
		0.005	10.8	107	0.0058
		0.010	9.66	109	0.0101
		0.022	8.43	110	0.0187
		0.047	6.05	112	0.0284
		0.072	4.94	114	0.0354
		0.096	4.33	114	0.0417
		0.138	3.66	115	0.0503
		0.179	3.14	116	0.0561
		0.220	2.85	116	0.0627
		0.282	2.55	118	0.0718
		0.426	2.06	119	0.0877
	6	0.000		114	0.0000
		0.005	9.71	115.6	0.0048
		0.010	8.55	117	0.0084
		0.022	6.8	118.8	0.0151
		0.047	5.22	119	0.0245
		0.072	4.18	121	0.0299
		0.096	3.64	119.5	0.0351
		0.138	3.07	121.2	0.0422
		0.179	2.74	125	0.0490
		0.220	2.45	124	0.0539
		0.282	2.2	126.35	0.0620
		0.426	1.74	127	0.0741

APPENDIX II: KEY WORDS OF ABAQUS INPUT FILE

*Connector Behavior, name=crease

*Connector Elasticity, nonlinear, component=4

-1.44,   0.

 -1.2, 0.174533

-0.96, 0.349066

-0.72, 0.523599

-0.48, 0.698132

-0.24, 0.872665

  0.,   1.0472

 0.24, 1.22173

 0.48, 1.39626

 0.72, 1.5708

 0.96, 1.74533

 1.2, 1.91986

 1.44, 2.0944

 1.68, 2.26893

 1.92, 2.44346

 2.16, 2.61799

 2.4, 2.79253

 2.64, 2.96706

 2.88, 3.14159

*Connector Damping, component=4

0.001,

*Amplitude, name=smoothstep, definition=SMOOTH STEP

          0.,   0.,   1.,   1.

** INTERACTION PROPERTIES

*Surface Interaction, name=IntProp-1

*Friction

0.,

*Surface Behavior, pressure-overclosure=HARD

** BOUNDARY CONDITIONS

** Name: pinned edge Type: Displacement/Rotation

** LOADS

** Name: viscous pressure   Type: Pressure

*Dsload

_PickedSurf25, VP, 1e-07

** INTERACTIONS

** Interaction: Int-1

*Contact, op=NEW

*Contact Inclusions, ALL EXTERIOR

*Contact Property Assignment

, , IntProp-1